This is the peer reviewed version of the following article:

A network of macrophages supports mitochondrial homeostasis in the heart

José A. Nicolás-Ávila[1,25], Ana V. Lechuga-Vieco[1,2,25], Lorena Esteban-Martínez[1], María Sanchez-Díaz[1], Elena Díaz-García[1], Demetrio J. Santiago[1], Andrea Rubio-Ponce[1], Jackson LiangYao Li[1,3], Akhila Balachander[3], Juan A. Quintana[1], Raquel Martínez-de-Mena[1], Beatriz Castejón-Vega[4], Andrés Pun-García[1], Paqui G. Través[5], Elena Bonzón-Kulichenko[1,6], Fernando García-Marqués[1], Lorena Cussó[1,7,8,9], Noelia A-González[1,10], Andrés González-Guerra[1], Marta Roche-Molina[1], Sandra Martin-Salamanca[1], Georgiana Crainiciuc[1], Gabriela Guzmán[1,11], Jagoba Larrazabal[1], Elías Herrero-Galán[1], Jorge Alegre-Cebollada[1], Greg Lemke[5], Carla V. Rothlin[12], Luis Jesús Jimenez-Borreguero[6,13], Guillermo Reyes[13], Antonio Castrillo[14,15,16], Manuel Desco[1,7], Pura Muñoz-Cánoves[1,17,18], Borja Ibáñez[1,6,18], Miguel Torres[1], Lai Guan Ng[3], Silvia G. Priori[1,20,21], Héctor Bueno[1,6], Jesús Vázquez[1,6], Mario D. Cordero[4,22,23], Juan A. Bernal[1], José A. Enríquez[1,24,26,*] and Andrés Hidalgo[1,26,*,#]

[1] Centro Nacional de Investigaciones Cardiovasculares Carlos III, Madrid 28029, Spain

[2] CIBER de enfermedades respiratorias (CIBERES), Madrid 28029, Spain

[3] Singapore Immunology Nework (SIgN), A*STAR, Biopolis, Singapore 138648, Singapore

[4] Oral Medicine Department, University of Sevilla, Seville 41009, Spain

[5] Molecular Neurobiology Laboratory, the Salk Institute for Biological Studies, La Jolla, California 92037, USA

[6] CIBER de enfermedades cardiovasculares (CIBERCV), Madrid 28029, Spain

[7] Departamento de Bioingeniería e Ingeniería Aeroespacial, Universidad Carlos III de Madrid, Madrid 28911, Spain

[8] Instituto de Investigación Sanitaria Gregorio Marañón, Madrid 28009, Spain

[9] Centro de Investigación Biomédica en Red de Salud Mental (CIBERSAM), Madrid 28029, Spain

[10] Institute of Immunology, University of Muenster, Muenster 48149, Germany

[11] Hospital Universitario La Paz, IdIPaz, Madrid 28046, Spain

[12] Departments of Immunobiology and Pharmacology, Yale University, New Haven CT 06520, USA

[13] Hospital Universitario de La Princesa, Madrid 28006, Spain

[14] Instituto Investigaciones Biomédicas "Alberto Sols", CSIC-UAM, Madrid 28029, Spain

[15] Unidad de Biomedicina IIBM-Universidad de las Palmas de Gran Canaria (ULPGC) (Unidad Asociada al CSIC), Las Palmas 35001, Spain

[16] Instituto Universitario de Investigaciónes Biomédicas y Sanitarias, ULPGC, Las Palmas 35016, Spain

[17] Department of Experimental & Health Sciences, Universitat Pompeu Fabra, CIBERNED, Barcelona 08003, Spain

[18] ICREA, Barcelona 08908, Spain.

[19] IIS- Fundación Jiménez Díaz Hospital, Madrid 28040, Spain

[20] Molecular Cardiology, ICS-Maugeri IRCCS, Pavia 27100, Italy

[21] Department of Molecular Medicine, University of Pavia, Pavia 2700, Italy

[22] Cátedra de Reproducción y Genética Humana del Instituto para el Estudio de la Biología de la Reproducción Humana (INEBIR) y la Universidad Europea del Atlántico (UNEATLANTICO), Seville 41009, Spain

[23] Fundación Universitaria Iberoamericana (FUNIBER), Barcelona 08005

[24] CIBER de fragilidad y envejecimiento saludable (CIBERFES), Madrid 28029, Spain

[25] These authors contributed equally.

[26] Senior authors

* Correspondence: Andrés Hidalgo (ahidalgo@cnic.es) and José Antonio Enríquez (jaenriquez@cnic.es)

[#] Lead Contact: Andres Hidalgo (ahidalgo@cnic.es)

Area of Cell & Developmental Biology, Fundación CNIC, Calle Melchor Fernández Almagro 3, 28029 Madrid, Spain. Phone: +34 91 4531200 (Ext. 1504). Fax: +34 91 4531245

Summary

Cardiomyocytes are subjected to the intense mechanical stress and metabolic demands of the beating heart. It is unclear whether these cells, which are long-lived and rarely renew, manage to preserve homeostasis on their own. While analyzing macrophages lodged within the healthy myocardium, we discovered that they actively took up material, including mitochondria, derived from cardiomyocytes. Cardiomyocytes ejected dysfunctional mitochondria and other cargo in dedicated membranous particles reminiscent of neural exophers, through a process driven by the cardiomyocyte's autophagy machinery that was enhanced during cardiac stress. Depletion of cardiac macrophages or deficiency in the phagocytic receptor Mertk resulted in defective elimination of mitochondria from the myocardial tissue, activation of the inflammasome, impaired autophagy, accumulation of anomalous mitochondria in cardiomyocytes, metabolic alterations, and ventricular dysfunction. Thus, we identify an immune-parenchymal pair in the murine heart that enables transfer of unfit material to preserve metabolic stability and organ function.

Introduction

Macrophages are now known to be endowed with tissue-specific tasks unrelated to immunity (Davies et al., 2013). These functions are prominent in the heart, where tissue-resident macrophages have been shown to prevent fibrosis (Chakarov et al., 2019), facilitate electrical conduction in the atrioventricular node (Hulsmans et al., 2017), or to favour healing of injured areas (Dick et al., 2019; Nahrendorf and Swirski, 2013). Macrophages of unknown function also populate other regions of the healthy heart, including the ventricular myocardium (Pinto et al., 2012), suggesting broader homeostatic functions for heart-resident macrophages.

A primary function of macrophages is to eliminate unwanted material through phagocytosis (Gordon, 2016). Illustrative of the relevance of this process, billions of cells die daily in healthy organisms yet few apoptotic or dead cells can be detected in tissues (Lemke, 2019). Atypical modalities of phagocytosis also exist in which cellular fragments containing dysfunctional organelles are ejected for disposal (Melentijevic et al., 2017), and have been mostly described in the central nervous system where it may allow stressed cells to dispose of damaged material. Whether similar mechanisms exist in the heart, an organ subjected to high metabolic or mechanical stress, remains unexplored.

Cardiomyocytes are highly specialized in function and structurally unique; they display large sizes and a tight distribution of organelles, including mitochondria and sarcomeres, which occupy most of the cell volume and deal with the intense metabolic and mechanical demands of the heart. These demands are additionally challenging for cardiomyocytes because their estimated turnover

3

in adult hearts is extremely low (Bergmann et al., 2009), suggesting that dedicated mechanisms may have evolved to support cardiomyocyte function. Here, we show that cardiomyocytes partly solve these challenges through ejection of mitochondria and other material in subcellular vesicles. Efficient uptake of these vesicles by macrophages through the receptor Mertk, in turn, prevents extracellular accumulation of waste material, inflammasome activation and autophagic block, altogether supporting heart homeostasis.

Results

A network of resident macrophages supports cardiac function

We focused on cardiac-resident macrophages (cMacs) which have been previously defined as CD45+ CD11b+ F4/80+, and three subsets originally defined on the basis of MHCII and Ly6C expression (Epelman et al., 2014; Molawi et al., 2014) (Fig.S1A). cMacs were of myeloid origin as determined by GFP expression in CX3CR1^{GFP}, Csf1r^{GFP} and LysM^{GFP} reporter mice (Burnett et al., 2004; Faust et al., 2000; Hulsmans et al., 2017; Jung et al., 2000) (Fig.S1B). To examine the global distribution of cMacs in detail, we cleared hearts from healthy heterozygous CX3CR1^{GFP} adult male mice for whole-organ imaging. GFP+ cMacs were ubiquitously distributed (Figure 1A, Fig.S1C and Video S1), with an estimate of about 3 x 10^5 cells per heart. cMacs were present at high density in the myocardium, around both ventricles (Figure 1A). High-resolution imaging of thick heart sections of genetic mosaics of tdTtomato+ cardiomyocytes or CX3CR1^{GFP} mice revealed that on average each cardiomyocyte was surrounded by five cMacs, and that each cMac interacted with up to five cardiomyocytes through cellular processes (Figure 1B, Fig.S1D-E and Video S2), a finding that suggested parenchymal-immune crosstalk in the heart, and potential housekeeping functions for cMacs.

To explore the possible housekeeping functions of cMacs, we examined the consequences of their depletion in heart physiology. Among cardiac cells, only cMacs expressed the sialoadhesin CD169/*Siglec1* (Fig.S1F) and we therefore took advantage of mice expressing the diphtheria toxin receptor (DTR) under this locus (CD169^{DTR} mice (Miyake et al., 2007)) to deplete cMacs from adult hearts (Fig.S1G), without affecting other cardiac cell populations (not shown). Although the CD169^{DTR} model depletes macrophages in several organs, we did not find evidence of systemic inflammation or overt damage to other organs (Table S1). Proteomic analysis of the myocardium at different times of cMac-depletion revealed global changes in protein composition over time (Figure 1C). These changes primarily affected mitochondrial proteins involved in bioenergetics, reactive oxygen species (ROS) and proteostasis (Figure 1D and Fig.S1H). Interestingly, although many mitochondrial proteins were less represented after cMac-depletion (Fig.S1H), transmission electron microscopy (TEM) imaging revealed a significant increase in the number of mitochondria

within cardiomyocytes, which we confirmed by immunostaining for mitochondrial protein Tom20 in heart sections (Figure 1E and Fig.S1I-J). Citrate synthase activity, an independent measure of mitochondrial mass, confirmed increased mitochondria content in the heart but not in the liver (Fig.S1K), despite efficient depletion of macrophages in both tissues (Fig.S1L). In addition to changes in number, mitochondria presented conspicuous alterations in morphology featuring increased area and reduced cristae density (Figure 1F), which suggested compromised fitness of cardiac mitochondria in the absence of cMacs. Accordingly, ATP production by purified cardiac mitochondria was significantly reduced in cMac-depleted mice regardless of the substrate used (Figure 1G), but was unaffected in the liver (Fig.S1M), indicating that the effects were tissue-specific. Extracts of cMac-depleted hearts showed ATPase β-subunit / GAPDH ratios (bioenergetic cellular index or BEC (Cuezva et al., 2004), Fig.S1N), which aligned with increased phosphocreatine-to-ATP ratios (PCr/ATP) in living hearts, as measured by magnetic resonance spectroscopy (^{31}P-MRS; Fig.S1O). In functional terms, these findings suggested that depletion of cMacs promoted a metabolic switch towards preferential use of glucose for energy production, to compensate for defective oxidative phosphorylation and reduced ATP stores. Consistent with this notion, *in vivo* uptake of the glucose analogue 2-deoxy-2-(18F)-fluoro-D-glucose (^{18}F-FDG) was elevated in cMac-depleted hearts (Figure 1H). Thus, hearts depleted of cMacs become defective at generating ATP and are metabolically unstable.

We next examined the effect of cMac depletion in left ventricular function. Longitudinal analyses of mice by echocardiographic imaging (Figure 1I-J) revealed loss of left ventricular volume and progressive reductions in E/A wave ratios, indicating diastolic dysfunction (Figure 1I). We additionally found reduced cardiac outputs after cMac-depletion (Figure 1J), indicating that systolic function was also affected. Finally, direct hemodynamic analysis of cMac-depleted hearts confirmed the diastolic dysfunction, as reflected by reduced -dP/dtmin and Tau Weiss values (a measure of relaxation properties), and systolic defects shown by reduced dP/dtmax and end-systolic pressure (Figure 1K). Interestingly, depletion of cMacs followed by a recovery period resulted in restoration of left ventricular volume, E/A ratios, and cardiac output when cMacs repopulated the heart (Fig.S1P-Q). Altogether, these data indicated that macrophages are needed for mitochondrial fitness, ventricular proteostasis, and pumping function.

Active phagocytosis by cardiac-resident macrophages

Given the constant mechanical stress of the myocardium, we speculated that cMacs might facilitate removal of damaged cells. Consistently, isolated cMacs, but not cardiac monocytes, featured large phagolysosome-like vacuoles indicative of active phagocytosis (Fig.S2A). To explore the phagocytic activity of cMacs, we first used bone marrow transplantation to generate chimeric mice

in which we confirmed transfer of fluorescent material from the parenchyma into macrophages by flow cytometry (Figure 2A and Fig.S2B) (A-Gonzalez et al., 2017). To define the origin of the phagocytosed material, we generated various models in which only circulating leukocytes (parabiosis; (A-Gonzalez et al., 2017)), endothelial cells (Cadh5^{CreERT}; Rosa26^{TdTom} mice), or cardiomyocytes (αMHC^{Cre}; Rosa26^{TdTom} mice, referred to as Card^{RED} mice) expressed red fluorescent protein. We found that cMacs took up abundant fluorescent material from circulating cells and from cardiomyocytes and, to a lesser extent, endothelial cells (Figure 2B and Fig.S2C). Monocytes, in contrast, incorporated little fluorescence (Figure 2A-B), altogether revealing that cMacs actively and specifically take up material from surrounding cardiac cells in the steady-state.

Cardiac exophers transport mitochondria

Uptake of cardiomyocyte-derived material was surprising given the low death rates of these cells in healthy individuals (Bergmann et al., 2009). We therefore examined the source of cardiomyocyte-derived material in Card^{RED} mice. We found numerous subcellular particles (11.5 ± 1.3 per 100 μm^2 tissue; Figure 2C-D and Video S3) whose tdTomato+ fluorescence indicated a cardiomyocyte origin; we refer to these particles as *cardiac exophers*, in analogy to structures reported in *C. elegans* neurons (Melentijevic et al., 2017). Cardiac exophers were relatively homogenous in size (mean diameter 3.5 ± 0.1 μm; mean volume 31.0 ± 2.5 μm^3), much smaller than cardiomyocytes (~0.2% of their volume, as estimated from (Bensley et al., 2016)) or cMacs (Fig.S2D). Around 40% of exophers were in contact with or inside cMacs (Figure 2C-E, Fig.S2E and Video S3), indicating that they were part of the phagocytosed material. The proximity of exophers to cMacs could not be explained by random distribution (Fig.S2F), and we ruled out horizontal transfer of tdTomato-encoding mRNA to cMacs as a mechanism of fluorescence acquisition (Fig.S2G), altogether suggesting uptake of cardiomyocyte-derived exophers by cMacs in the healthy myocardium.

TEM of heart sections revealed conspicuous presence of mitochondria (Figure 2F) and, in some instances, sarcomeric fragments inside extracellular exopher-like vesicles (Fig.S2H). We found similar structures and cMacs in human myocardia (Fig.S2I-J and Table S2). To characterize the content of these particles, we purified exophers as small tdTomato^{bright} particles devoid of nuclei from pools of hearts of Card^{RED} mice (Fig.S2K-L). Staining with two different probes that accumulate in the mitochondrial matrix confirmed the presence of mitochondria in isolated exophers (Figure 2G), and comparison of the proteome of purified exophers with that of total cardiac tissue revealed massive enrichment of mitochondrial proteins, and reduction in proteins from all other cellular compartments (Figure 2H and Fig.S2M). Intriguingly, we noted that several proteins involved in mitochondrial integrity were reduced in exophers, including Opa1, Fis1, Cytc

and Aifm1 (Fig.S2M), suggesting that mitochondria within exophers might be dysfunctional (Duvezin-Caubet et al., 2006; Joza et al., 2001; Mai et al., 2010). We confirmed the proteomic data by immunofluorescence staining of myocardial tissue, with consistent presence in exophers of mitochondrial and sarcomeric proteins, proteins from various other organelles, and absence of DAPI+ nuclear fragments (Figure 2I-J and Fig.S2N). These data thus revealed preferential, but not exclusive, extrusion of mitochondria into exophers for discharge from healthy cardiomyocytes.

Elimination of cardiomyocyte-borne mitochondria by cMacs

Our TEM analyses revealed mitochondria-containing exophers in the periphery of cardiomyocytes that were taken up by adjacent cells similar in size and morphology with cMacs (Hulsmans et al., 2017) (Figure 3A). Consistently, 3D immunofluorescence imaging revealed Tom20+ exophers inside CD68+ cMacs (Figure 3B-C and Video S3), suggesting exopher-mediated transfer of mitochondria from cardiomyocytes to cMacs.

To confirm this, we used two complementary strategies. We first transplanted BL/6.SJL^{C57} mice with bone marrow from conplastic BL/6^{NZB} donor mice. These mouse strains have C57BL/6 nuclear genomes, but distinct mitochondrial DNA haplotypes (C57 and NZB, respectively (Latorre-Pellicer et al., 2016)) that can be discriminated by restriction fragment length polymorphism (RFLP) assays. These mice also expressed different isoforms of CD45 that discriminated donor from recipient-derived cMacs, thereby allowing identification of parenchyma-derived mitochondria in the transplanted cMacs (Fig.S3A). cMacs from BL/6^{NZB} donors purified from BL/6.SJL^{C57} hearts incorporated parenchymal C57-derived mtDNA at much higher rates than macrophages from any other tissue tested (Figure 3D). Only the skeletal muscle revealed low transfer of mtDNA, thereby indicating strong heart-specific transfer of parenchymal mitochondria into cMacs.

To determine whether cardiomyocytes were the source of mitochondria transferred to cMacs, we next analysed the transfer of cardiomyocyte-borne mitochondrial protein. We enforced expression of a monomeric Keima fluorescent protein bearing a mitochondria-directing peptide (mt-Keima) in cardiomyocytes (Fig.S3B and (Sun et al., 2015)). We ensured cell-specific transduction by using a cardiotropic adeno-associated virus 9 (AAV9) and the cardiomyocyte-specific *Tnnt2* promoter to drive mt-Keima expression in cardiomyocytes but not in cMacs (Fig.S3B-C). Immunofluorescence staining revealed the presence of mt-Keima in exophers (Fig.S3D-E), and abundant mt-Keima+ particles that concentrated inside CD68+ macrophages (Figure 3E-F and Video S4), indicating transfer of cardiomyocyte-borne mitochondria into cMacs.

mt-Keima protein changes excitation wavelength at different pH, thus changing fluorescence when entering phagolysosomes (Sun et al., 2017). We found that mt-Keima within cMacs presented fluorescence ratios indicative of a more acidic environment (Fig.S3F), suggesting that they were

7

targeted for degradation in these cells. Consistently, the majority of mt-Keima+ mitochondria in cMacs were in Lamp1+ phagolysosomes (Fig.S3G and Video S4). In addition, cMacs isolated from mt-Keima-transduced hearts, or from BL/6^{NZB}-transplanted BL/6.SJL^{C57} mice, lost most of the mt-Keima fluorescence or BL/6^{NZB} mtDNA after only 2 or 3 days of culture, respectively (Figure 3G), indicating degradation of the engulfed mitochondria. Finally, we found that the majority of acidic mt-Keima+ particles in the myocardium localized inside cMacs (62.7 ± 9%; Fig.S3H), and *in vitro* imaging revealed exchange of exopher-like particles between cardiomyocytic cells and FACS-purified cMacs (Fig.S3I-K and Video S5). Thus, a large fraction of mitochondria extruded in exophers are taken up and eliminated by neighbouring macrophages.

Exopher formation is driven by cardiomyocyte autophagy

Given the consistent reduction of components associated with mitochondrial fitness in our proteomic analysis (Fig.S2M and Fig.S4A), and the observation that peripheral mitochondria often accumulated in budding vesicles in the periphery of cardiomyocytes (Fig.S4B), we hypothesized that exophers allowed disposal of dysfunctional mitochondria. Using a binary criteria to score mitochondrial fitness from TEM images as normal or abnormal based on outer and inner membrane integrity, cristae density and organization (Fig.S4C), we found a progressive decline in fitness from perinuclear to border regions of the cardiomyocyte, with the highest frequency of aberrant mitochondria in exophers (Fig.S4D-E). This finding agreed with dramatic disruption of the membrane potential and unresponsiveness to hyperpolarizing agents (Fig.S4F), as well as reduced citrate synthase (Fig.S4G), of mitochondria present in exophers, indicating that damaged mitochondria accumulate in the periphery of cardiomyocytes, and are ejected in exophers.

These findings raised the possibility that exopher production was related to autophagy, an evolutionarily-conserved system that mediates disposal of organelles. Consistently, we found LC3+ positive puncta (which identify autophagosomes (Mizushima et al., 2004)) in the majority of exophers present in heart sections and by flow cytometry in isolated exophers (Figure 4A-B). To assess a role for autophagy in exopher formation, we next used two complementary strategies. First, we induced autophagy through inhibition of mTOR with rapamycin. Second, we specifically blocked autophagy in cardiomyocytes by genetic deletion of *Atg7* (García-Prat et al., 2016) (Figure 4C). Treatment of Card^{RED} mice with rapamycin increased exopher numbers in the myocardium (Figure 4D) and enhanced the uptake of cardiomyocyte-derived fluorescence and mt-Keima by cMacs (Figure 4E-F). We then impaired cardiac-specific autophagy by deletion of one *Atg7* allele from cardiomyocytes, a manipulation that led to suppression of autophagy flux, yet allowed better survival than full gene deletion (Fig.S4 H-I). Hemizygous mice manifested dramatic reduction of cardiac exophers (Figure 4G), which was accompanied by reduced uptake of cardiomyocyte-

derived fluorescent protein and mt-Keima by cMacs (Figure 4H-I). Thus, exopher formation and mitochondrial transfer is driven by the autophagy machinery of cardiomyocytes.

Exopher clearance by cMacs prevents inflammasome activation and autophagy block

Disposal of mitochondria-laden exophers by cMacs suggested that they might prevent accumulation of inflammogenic material in the myocardial tissue, and downstream detrimental effects seen when cMacs were depleted (Figure 1C-K). To explore this possibility, we generated and imaged hearts from CD169^{DTR}; aMHC^{Cre}; Rosa26^{tdTom} mice to score exopher content after cMac depletion. As expected by their role in taking up these vesicles, exopher content doubled after only two days of cMac depletion (Figure 5A), and there was marked accumulation of free mitochondria in the cardiac extracellular space after long-term macrophage depletion (Figure 5B and Fig.S5A).

Unexpectedly, we noticed that depletion of cMacs for longer times resulted in progressive decline in exopher numbers, with almost complete absence of exophers after three weeks (Figure 5A). Because autophagy drives exopher production (Figure 4), we hypothesized that prolonged cMac depletion might interfere with cardiomyocyte autophagy, thereby impairing exopher production. Analysis of isolated cardiomyocytes confirmed that sustained depletion of cMacs (7 to 21 days) completely blocked the autophagy flux (Figure 5C and Fig.S5B), whereas short-term depletion (2 days) did not (Fig.S5C). Combined, these data suggested that while cMacs are not directly involved in eliciting exopher release by cardiomyocytes, they are necessary to sustain normal cardiac autophagy. Hence, long-term depletion of cMacs blunts exopher production and cause proteostatic defects and proteome alterations in cMac-depleted hearts (Figure 1C-D).

Free mitochondria and mtDNA can activate the inflammasome and elicit cardiac damage (Oka et al., 2012; Zhou et al., 2011); in agreement with this possibility, Western blot analyses revealed inflammasome activation in hearts of cMac-depleted mice (Figure 5D). Inflammasome activation, in turn, can inhibit autophagy (Yu et al., 2014), raising the possibility that impaired mitochondria removal and inflammasome activation in the absence of cMacs caused the observed autophagic arrest and impaired exopher production. Indeed, inhibition of the NLRP3 inflammasome in cMac-depleted mice using the small-molecule inhibitor MCC950 (Fig.S5D and (Coll et al., 2015)) rescued the autophagic block (Figure 5E), and partially restored exopher formation in hearts from these mice (Figure 5F). These data are consistent with a model in which cMacs preserve cardiomyocyte proteostasis by removing cardiac exophers, thereby preventing inflammasome activation and autophagy block. These housekeeping roles of cMacs may ultimately explain the dramatic impact of their depletion in mitochondrial quality and cardiac function (Figure 1C-K).

Cardiac stress stimulates mitochondrial transfer

We next questioned the capacity of exopher-mediated disposal of mitochondria to adapt to situations of cardiac stress. We treated Card^{RED} mice with isoproterenol, a β-adrenergic agonist that causes cardiomyocyte damage through mitochondrial stress (Acin-Perez et al., 2018). Isoproterenol treatment induced loss of mitochondrial quality in cardiomyocytes as assessed by TEM analysis (Figure 6A-B), and this was paralleled by a marked increase in the number of cardiac exophers (Figure 6C), as well as elevated transfer of cardiomyocyte-derived fluorescence and mt-Keima into cMacs (Figure 6D-E), thereby revealing a dynamic response of exopher-mediated transfer of mitochondria during cardiac stress. We also analysed hearts after myocardial infarction in Card^{RED} mice. Although analyses involving cMacs were not possible after cardiac ischemia given the massive infiltration of inflammatory macrophages in regions devoid of cardiomyocytes (Fig.S6A), we found areas in the periphery of the infarcted myocardium that became enriched in cardiomyocyte-derived particles (Fig.S6B). These particles shared with exophers a similar morphology, presence of mitochondria, and absence of actin (Fig.S6C), suggesting elevated formation of cardiac exophers after ischemia. Consistent with the organ-supporting functions of cMacs (Figure 1), the effects of isoproterenol were more severe in cMac-depleted mice as revealed by echocardiography and creatinine kinase levels in plasma (Fig.S6D-E). Similarly, depletion of cMacs prior to ischemia resulted early mortality upon reperfusion (Fig.S6F). Thus, mitochondrial disposal through exophers occurs in a range of pathophysiological conditions, and is enhanced under conditions of stress.

The presence of mitochondria in exophers and transfer into cMacs in healthy hearts suggested that this might represent a homeostatic mechanism of disposal independent of organelle fitness. In contrast, the presence of dysfunctional mitochondria in border zones and exophers (Fig.S4D-G) suggested that exophers could alternatively allow sorting of defective mitochondria for elimination, thereby providing a mechanism of quality control. To evaluate these possibilities, we tested whether genetic protection from isoproterenol-induced stress in *Oma1*-deficient mice, which are protected from mitochondrial damage (Acin-Perez et al., 2018)), affected exopher formation. We found that preservation of mitochondrial quality in *Oma1*$^{-/-}$ mice blunted mitochondria transfer to cMacs in response to isoproterenol (Figure 6E), suggesting that exopher release by cardiomyocytes is causally associated with mitochondrial health.

The phagocytic receptor Mertk mediates exopher removal

Using flow cytometry, we noticed that exophers expressed on their surface phosphatidyl-serine (PS; Figure 7A), an "eat-me" signal typically found on apoptotic cells that is recognized directly or indirectly by various phagocytic receptors in macrophages. Among these, the tyrosine kinase Mertk has been shown to be active in cardiac macrophages (DeBerge et al., 2017; Wan et al., 2013), in which it was expressed at high levels (Fig.S7A-B), and mediates the removal of dysfunctional subcellular fragments in other tissues (Lemke, 2019). Using Annexin V as a probe, we found PS+ patches in fresh ventricular sections that were distributed through the myocardium in proximity to CX3CR1^{GFP} cMacs (Figure 7B-C). Importantly, transfer of cardiomyocyte-derived mt-Keima+ mitochondria into cMacs was severely compromised in $Mertk^{-/-}$ mice, even after controlling for mt-Keima transduction efficiency (Figure 7D). Consistently, we found accumulation of free mitochondria in the extracellular space of $Mertk$-deficient hearts (Figure 7E) despite higher number of cMacs in these mice (Fig.S7C), as well as activation of the inflammasome and blunted autophagy (Fig.S7D-F). These observations predicted mitochondrial alterations in cardiomyocytes from $Mertk^{-/-}$ mice; indeed, we found that cardiomyocytes displayed increased mitochondrial content (Figure 7F and Fig.S7G), but these mitochondria featured reduced cristae density (Figure 7G) and diminished ATP production that was evident in older $Mertk^{-/-}$ mice (Fig.S7H). These data indicated loss of mitochondrial quality and suggested alterations in the functional and metabolic properties of $Mertk$-deficient hearts. Accordingly, echocardiographic analyses revealed reduced left ventricle E/A ratios (Fig.S7I), and PET/CT imaging demonstrated increased in $vivo$ uptake of ^{18}F-FDG compared with wild-type controls (Figure 7H), thereby recapitulating the defects seen in cMac-depleted hearts (Figure 1H-I). Thus, Mertk is a relevant receptor for exophers, and its absence causes accumulation of dysfunctional mitochondria and metabolic anomalies in the heart.

Discussion

The massive energetic demand of the heart make this organ uniquely reliant on a vast pool of functional mitochondria to continuously generate high-energy phosphates. Mechanisms that ensure mitochondrial health in cardiomyocytes, including elimination of dysfunctional mitochondria by mitophagy, are therefore crucial for cardiac function and have been the focus of intense scrutiny (Tong and Sadoshima, 2016). Existing models, however, assume that disposal of mitochondria and other intracellular material is completed within the cell; an assumption with important implications in terms of the involved molecular mediators, turnover rates, energetic cost, and potential activation of danger sensors in the heart. Here, we identify a non-canonical route for elimination of a large fraction of mitochondria and other organelles from healthy cardiomyocytes that is driven by components of the autophagy machinery, yet uniquely relies in membranous structures (exophers) for extrusion of cellular waste, including abnormal mitochondria, into the extracellular space. The extruded material is readily taken up and processed by a network of

resident macrophages that surround cardiomyocytes, through the phagocytic receptor Mertk. Failure to eliminate mitochondria-laden exophers results in activation of the inflammasome and autophagy arrest, ultimately compromising mitochondrial fitness, tissue proteostasis, and cardiac function.

A key observation was the detection in the healthy myocardium of cardiomyocyte-derived fragments, which was surprising as these fragments originated from otherwise viable cells, and were enriched in damaged mitochondria. These vesiculated fragments had properties that differentiate them from classical extracellular vesicles (Colombo et al., 2014), including size (in the range of microns), cargo (large organelles) and mechanism of formation (autophagy vs. endosomal origin). Instead, these cardiomyocyte-derived fragments shared traits with neural exophers, most notably the capacity to transport cargo for disposal out of the cell (Melentijevic et al., 2017). These features suggest a specialized function for exophers in supporting cardiac proteostasis.

Our findings have a number of potential implications. First, they reveal that autophagy in the mammalian heart can be completed by exchange of material between cells, a trans-cellular process so far reported only in certain areas of the central nervous system (Davis et al., 2014). Second, they predict the existence of biochemical mediators in cardiomyocytes dedicated to sort unfit mitochondria and other material to exophers for ejection out of the cell. Third, our findings establish a central, previously-undescribed role for heart-resident macrophages in preserving cardiac homeostasis beyond those related to electrical conductance (Hulsmans et al., 2017), the only homeostatic role thus far reported for cMacs in the healthy heart. A technical limitation of our study was the inability to specifically deplete cardiac macrophages due to the lack of a tissue-specific model, and therefore we cannot formally exclude the possible influence of CD169+ macrophages from other organs in cardiac physiology.

We propose that this unique type of "subrogated" elimination of cellular waste from cardiomyocytes to cMacs may be a necessary feature of the heart that originates from the physiological constraints of the cardiomyocyte, a cell that must function uninterruptedly throughout the organism's lifetime, and features a tightly-packed cytoplasm that may hamper efficient autophagy. In light of these constraints, it is not surprising that assisted elimination of the most abundant organelle, i.e. mitochondria, by neighboring cMacs ensures mitochondrial and cardiomyocyte fitness, while failure of this mechanism, as may occur during aging, could compromise organ function (Rawji et al., 2016).

Phagocytosis of subcellular particles from otherwise viable cells has been reported under specific contexts and tissues, and typically allows cells to get rid of dysfunctional or unnecessary structures, as seen for maturing erythrocytes and sperm, or for some types of neurons (Lemke, 2019). Thus,

while there exist precedents for material ejection from living cells and transfer to neighboring cells (Melentijevic et al., 2017), the heart appears unique in the massive amount of exchanged material, which accounts for more than half of all mitochondria, and the preference of this process towards a type of organelle (the mitochondria). We predict, nonetheless, that similar dependence on exopher production and uptake by neighboring macrophages may occur in other populations of long-lived cells subjected to constant physiological stress. For example, the absence of Mertk is causally associated with defective removal of photoreceptor outer segments from viable cells in the retina, resulting in blindness (Lemke, 2019). Genetic models that enable tracking mitochondria or other organelles from specific sources to tissue-resident macrophages will be needed to define the prevalence of this mechanism in tissues not explored in our study.

In summary, identification of active elimination of cardiomyocyte-derived mitochondria and other material by surrounding cMacs establishes a paradigm for how resident phagocytes contribute to global tissue homeostasis. It also predicts that cardiac dysfunction may, in some instances, emanate from defects in resident immune cells, rather than from cardiomyocytes, a concept with important consequences for the diagnosis and treatment of heart disease.

Acknowledgments

Author contribution

J.A.N-A, A.V.L-V, L.E-M., M.S-D., E.D., D.J.S., P.G.T., F.G-M., E.B-K., N.A-G., S.M-S, J.A.Q., R.M.dM., A.G-G., G.C., B.C-V., M.R-M., and E.H. performed experiments. A.R-P, J.L.L., E.B-K., J.J.B., G.G. and L.C. performed "omics", imaging, echocardiographic, electrocardiographic and PET-CT analyses, respectively. H.B. interpreted the echocardiographic analyses. J.A.N-A, J.A-C., G.L., J.V., S.G.P., J.A.B., J.A.E., M.D. and A.H. designed and supervised experiments. G.R. obtained human samples. A.C., C.V.R and P.M. contributed essential reagents. M.T., M.D., A.H. and J.A.E. designed and supervised the study. A.H., J.A.E. and J.A.N-A wrote the manuscript, which was edited by all authors.

Declaration of interest

The authors declare no competing interests.

Main figures titles and legends

Figure 1. cMacs support mitochondrial homeostasis and function in the heart.

(A) Distribution of cMacs in optically-cleared hearts from a CX3CR1[GFP] mouse after optical clearing and imaging by light sheet microscopy. Left, whole heart with each dot representing one GFP+ macrophage. Right, optical transversal sections (655 µm thick, indicated with numbers 1-5) pseudo-colored to display cMac densities. Far right, scheme showing the position of the left atrium (LA), left ventricle (LV), right ventricle (RV) and Septum (SP). The right atrium was not imaged. Scale bar, 1 mm. See also Video S1.

(B) 3D reconstruction of a large field in the left ventricle of a αMHC[CreERT]; Rosa26[TdTom] mouse one week after tamoxifen administration (left). Inset at right shows contacts between one cardiomyocyte (tdTomato+, red) and six cMacs (CD68, green). Images are representative of hearts from 4 mice. See also Video S2.

(C-D) Proteomic analyses of non-depleted control (Day0) and CD169[DTR] hearts at different times of cMac depletion. **(C)** Principal component analysis of control (day 0) and cMac-depleted mice (day 14 and 21). **(D)** Bubble plot representation of the most significantly changed canonical pathways when comparing hearts at days 0 vs. 21, using the Ingenuity Pathway Analysis tool.

(E) Representative TEM images in control and cMac-depleted mice (day 21). Mitochondria can be identified by higher electrodensity (dark areas). Scale bar, 10 µm.

(F) Reduced mitochondrial fitness in cMac-depleted mice (day 21) as defined from TEM images (left), and quantified as mitochondria area and percent of cristae area per mitochondria (right panels). Each dot represents one mitochondria; data are shown as means, from 300 mitochondria and 3 mice per group. ***, p<0.001 as determined by unpaired t-test.

(G) Ex vivo ATP production rates in isolated mitochondria in control and cMac-depleted mice (day 21) in the presence of the indicated substrates (glutamate/malate, succinate or palmitate/carnitine). Values are normalized to the respective controls and represented as Box and Whisker plots; data from 6-11 mice per group. **, p<0.01; ***, p<0.001; as determined by unpaired t-test.

(H) PET-CT images of ^{18}F-FDG uptake by hearts from non-depleted control and cMac-depleted mice. Image quantification is shown as box and whisker and given as standard uptake values (SUV; right); data from 7-13 mice per group. **, p<0.01 as determined by unpaired t-test.

(I) Experimental scheme of cardiac function analysis by echocardiography, at different times of cMac depletion (left). Right shows selected cardiac parameters measured by echocardiography in control and cMac-depleted mice (CD169[DTR]+ DT) at different times of DT treatment. Data are mean ± SEM normalized to day 0, from 12-21 mice per group. *, p<0.05; ** p<0.01; ***, p<0.001; n.s., not significant, as determined by Student's t-test analysis against day 0. LV, left ventricle; Vol, volume; EF, ejection fraction.

(J) Cardiac output as measured by echocardiography. Box and whisker plots show data from 12-21 mice per group. ***, p<0.001 as determined by unpaired t-test.

(K) Intracardiac hemodynamics in non-depleted control and cMac-depleted mice (CD169[DTR]+DT) after 3 weeks of treatment. Values for those parameters indicative of systolic (right), or diastolic function (left) are shown. Parameters represented are Left ventricular end-systolic pressure (LVESP), maximal derivative of LV pressure (dP/dtmax) and minimal derivative of LV pressure (-dP/dtmin). Data shown as box and whisker plots; n=5-6 mice. *, p<0.05; **, p<0.01; ***, p<0.001; as determined by unpaired t-test.

Controls for all cMac-depletion experiments were wild-type mice treated with DT.

Figure 2. Cardiac exophers transport mitochondria.

(A) Scheme of bone marrow transplantation (BMT; left) and percentage of cMacs that phagocytose DsRed+ material from parenchymal cells in the hearts of transplanted WT^{RED} mice.

(B) Experimental schemes (left) and percentage of cells that engulf DsRed- or Tomato-positive material from circulating leukocytes, endothelial cells or cardiomyocytes as determined in WT^{RED} with CD45.1 parabionts, Cadh5^{CreERT} Rosa26^{TdTom} mice or αMHC^{Cre} Rosa26^{TdTom} (Card^{RED}) mice, respectively. Bars in (A-B) show mean ± SEM from 3-6 mice per model. See also Fig.S2B-C

(C) Low and high magnification micrographs of hearts from Card^{RED} mice, illustrating the presence of cardiomyocytes and cardiomyocyte-derived exophers (white arrowheads) proximal to cMacs (CD68, green). Nuclei are shown in blue (DAPI).

(D-E) (D) 3D reconstructions from confocal images showing cardiomyocyte-derived exophers (red), some of which appear inside a cMac **(E)**; See also Video S3. Images are representative of 4 mice.

(F) TEM images of exopher-like vesicles in hearts of WT mice. Bottom images show enlarged details of areas in top images (dashed squares) that contain mitochondria. Images representative of 3 mice. Scale bars are indicated in the images.

(G) Cytometric analyses of purified exophers stained with the mitochondria-specific probes MitoTracker and MitoNIR. Histograms are representative of 5 mice from two experiments.

(H) Pie-charts showing the proteome composition of total cardiac tissue, and cardiac exophers. Data are from 3 samples per group. Proteins were quantified by the average number of spectral counts in the replicates and colors identify the cellular compartment from which the proteins originate, as shown in the legend.

(I) Representative images of left ventricular sections from Card^{RED} mice (tdTomato protein, red) stained for the indicated proteins (white) to assess their presence in exophers (yellow arrowheads).

(J) Fraction of exophers positive for the proteins shown in (I). Bars are mean ± SEM from 3-5 mice.

Figure 3. cMacs take up and eliminate cardiomyocyte-derived mitochondria.

(A) Pseudo-colored TEM images of a mononuclear cell (green) taking up mitochondria (brown) from a neighboring cardiomyocyte (yellow), at two different magnifications (dashed box).

(B) Micrograph of an exopher (arrowhead) containing Tom20+ material (white; left panel) in the heart of a Card^{RED} mouse; right panel shows a 3D reconstruction of the same image, illustrating the presence of Tom20+ mitochondria (grey) inside cardiomyocytes and cardiac exophers (transparent red). Images are representative of hearts from 4 mice.

(C) 3D reconstruction of a cMac from the heart of a Card^{RED} mouse containing cardiomyocyte-derived material, inside of which there are Tom20+ mitochondria. See also Video S3.

(D) Representative gels showing amplified C57 and NZB mtDNA, present in BL/6^{NZB}-derived macrophages isolated from the indicated tissues (left). Plots at right show the percent amount of C57-derived mtDNA in BL/6^{NZB} macrophages sort-purified from the same tissues; BM, bone barrow. Each dot is one mouse and bars show means; n= 3-20 mice per group. **, p<0.01; ***, p<0.001; n.s., not significant as determined by Kruskal-Wallis non-parametric test with multiple Dunn's comparison against Heart.

(E) Micrographs from hearts infected with AAV9-mt-Keima, showing a cluster of cardiomyocyte-derived mitochondria (mt-Keima+, red) inside a cMac (CD68+, green). Scale bars, 20 µm (left) or 10µm (right panels).

(F) 3D reconstruction of a cMac (CD68+, green) containing an mt-Keima+ particle (black); see also Video S4.

(G) Degradation of exogenous mitochondria by macrophages. cMacs were sort-purified from BL/6^{NZB} transplanted (C57 recipient) mice, or from wild-type mice infected with AAV9-mtKeima and set in culture and analyzed at the indicated times for the presence of C57-mtDNA or mt-Keima+ signal, respectively. The graph shows percentages of signal in cMacs over time, relative to time 0; data from one (keima) and two (mtDNA-NzB transplants) independent experiments. *, p<0.05; **, p<0.01; ***, p<0.001, as determined by multiple nonparametric Mann-Whitney test, against time 0.

Figure 4. Cardiomyocyte autophagy drives exopher production and mitochondrial transfer.
(A) Presence of GFP+ puncta revealing the presence of LC3 in exophers of Card^{RED}; LC3-GFP mice. Images representative of 3 mice.
(B) Detection of LC3-GFP in purified cardiac exophers by flow cytometry. Histogram is representative of 3 mice.
(C) Scheme of pathways leading to the formation of autophagosomes, which can be modulated by the mTOR inhibitor rapamycin, and relies on Atg proteins, including Atg7.
(D-F) Enhanced exopher production and mitochondrial transfer in rapamycin-treated mice. **(D)** Micrographs showing increased exophers as detected by immunofluorescence in Card^{RED} mice, with bars showing the number of exopher number per field of view (FOV); data from 4 mice per group. **(E)** Incorporation of cardiomyocyte-derived tdTomato signal into cMacs of vehicle or rapamycin-treated mice, as measured by flow cytometry (representative plots, left). Bars show mean fluorescence intensities (MFI) and percent of tdTomato+ cMacs; data from 4 mice per group. **(F)** Immunofluorescence images of AAV9-mt-Keima-transduced cardiomyocytes showing basic (458) or acidic (561) mt-Keima and macrophages, in control or rapamycin-treated mice; data from 5 mice per group. Graph at right shows mean ± SEM percentage of mt-keima+ mitochondria inside cMacs; n = 5 mice per group.
(G-I) Exopher production and mitochondria transfer in control Card^{RED}; $Atg7^{+/+}$ and αMHC^{CreERT}; $Atg7^{+/flox}$ mice. **(G)** Micrographs showing reduced exophers in Card^{RED}; $Atg7^{+/flox}$ mice, with bars depicting the number of exophers by field of view (FOV). Data from 4 mice per group. **(H)** Incorporation of cardiomyocyte-derived tdTomato signal into cMacs from $Atg7^{+/+}$ or $Atg7^{+/flox}$ mice, as measured by flow cytometry (representative plots, left). Bars show MFI and percent ± SEM of tdTomato+ cMacs; data from 9-10 mice per group. **(I)** Immunofluorescence images of AAV9-transduced cardiomyocytes showing basic (458) or acidic (561) mt-Keima and macrophages, in control or αMHC^{CreERT}; $Atg7^{+/flox}$ mice, four days after tamoxifen treatment; data from 4-5 mice per group. All bars show mean ± SEM, and statistical significance was determined using Student's t-test.

Figure 5. Exopher uptake prevents inflammasome activation and autophagy arrest

(A) Left, Representative micrographs of CD169^DTR; Card^RED hearts showing CD68+ cMacs (green) and exophers (arrowheads) after cMac-depletion for the indicated days. Right bar-graph shows exopher numbers as mean ± SEM per field of view; n = 4-8 mice per group. Scale bar, 20 µm. **, $p<0.01$; ***, $p<0.001$; n.s., not significant, as determined by Kruskal-Wallis with Dunn's multiple comparisons test against day 0.

(B) Left, representative TEM images of myocardia showing free mitochondria in the extracellular space of cMac-depleted hearts after 21 days of DT treatment (yellow arrowheads). Right, quantification of free mitochondria per field of view. *, $p<0.05$; as determined by nonparametric Mann Whitney analysis.

(C) Autophagy flux in isolated cardiomyocytes from wild-type control and cMac-depleted mice at day 21 of DT administration. Fluxes were measured by staining for LC3 (red) and nuclei (DAPI, blue) in basal and Hydroxychloroquine (HCQ)-treated cells. Bars show mean ± SEM of LC3+ particles per cardiomyocyte; n = 3 mice per group. Scale bar, 20 µm. *, $p<0.05$; n.s., not significant, as determined by Student t-test test.

(D) Levels of NLRP3, as well as precursor (pCasp1) and cleaved (cCasp1) forms of Caspase-1 protein in heart extracts of controls and cMac-depleted mice (21 days) as determined by western blot analyses. Bar graphs show mean ± SEM protein levels; n=7 mice per group from two independent experiments. **, $p<0.01$; ***, $p<0.001$ as determined by unpaired t-test.

(E) Autophagy flux in isolated cardiomyocytes from non-depleted control and cMac-depleted (21 days) mice, treated or not with MCC950. Bars show mean ± SEM of LC3+ particles per cardiomyocyte, from 3 mice per group. Scale bar, 20 µm. ***, $p<0.001$; n.s., not significant, as determined by one-way ANOVA.

(F) Left, experimental scheme to analyze exopher production in control and cMac-depleted mice (CD169^DTR Card^RED+ DT) treated or not with MCC950 for 21 days. Middle, representative micrographs and exopher quantification (right) in the same groups of mice. Bars show mean ± SEM exophers per field of view. Data are from 6 mice per group, from two independent experiments. **, $p<0.01$; ***, $p<0.001$; as determined by ANOVA with Tukey´s multiple comparisons test.

Controls for all cMac-depletion experiments were wild-type mice treated with DT.

Figure 6. Cardiac stress induces exopher production and mitochondrial uptake.

(A) TEM images of mitochondria in cardiomyocytes from mice treated chronically with isoproterenol or vehicle for 28 days. Note that mitochondria from isoproterenol-treated mice often displayed reduced cristae density and vacuolations (arrowheads). Scale bar, 0.5 µm. Images representative of 5 mice per group.

(B) Percentage of mitochondria classified as Abnormal (damaged outer membrane, voids, cristae or both) in regions defined as in Fig.S4D; data from 5 mice per group. *, p<0.05; ***, p<0.001 as determined by two-way ANOVA with Sidak's multiple comparison test.

(C) Representative micrographs showing exophers (white arrowheads; left), and quantification of exopher numbers in Card[RED] mice treated with vehicle or isoproterenol for one week. Bar graph shows mean ± SEM of exophers per field of view; data from 4 mice per group.

(D) tdTomato incorporation in cMacs in the same animals as in panel (C). Bars show mean ± SEM of tdTomato median fluorescence intensity (MFI) and percent of phagocytic cMacs (gated regions in plots); data from 4-8 mice per group.

(E) Representative micrographs and mt-Keima incorporation by cMacs in AAV9-infected WT or *Oma1*^{-/-} mice treated with isoproterenol or vehicle for one week. Bars show mean ± SEM percent mt-Keima inside cMacs, normalized to untreated controls; data from 4-12 mice per group. ***, p<0.001; n.s., not significant as determined by ANOVA with Dunn´s multiple comparisons test.

Figure 7. The phagocytic receptor Mertk mediates exopher removal

(A) Cytometry histograms of exophers from Card^RED mice stained for Annexin V or unstained.

(B) Slices of viable myocardium from CX3CR1^GFP mice showing the presence of PS patches (Annexin V; red) proximal to GFP+ cMacs. Insets show that Annexin V binding is calcium dependent (EDTA); Representative image from a total of 4 experiments.

(C) Bar graph shows distance distributions of Annexin V patches or Random dots to the closest cMac. Numbers indicate mean ± SEM distances for each group. Data from 16-32 images from 4 mice. P value was obtained by nonparametric Mann-Whitney test.

(D) Representative micrographs show cMacs (CD68, yellow), and cardiomyocyte-derived mitochondria (mt-Keima; cyan-red). Right, bar graphs show the percentage of mt-Keima+ signal inside cMacs in hearts from wild type and *Mertk*$^{-/-}$ mice infected with AAV9-Keima. Data are mean ± SEM from 5 mice per group. **, $p<0.01$; n.s., not significant as determined by non-parametric Mann Whitney analysis.

(E) TEM micrographs illustrating free mitochondria in the myocardia of wild type and *Mertk*$^{-/-}$ mice. Bars at right show the quantification of free mitochondria per field of view from the TEM images. Data are mean ± SEM from 3 mice per group. **, $p<0.01$ assessed by unpaired t-test.

(F) Representative TEM images of wild type and *Mertk*$^{-/-}$ hearts. Scale bar, 10 μm.

(G) TEM micrographs (left) and quantification of cristae area per mitochondria. Each dot represents one mitochondria and bars show means, from 15-20 images from 3-4 mice per group. **, $p<0.01$; as determined by nonparametric Mann-Whitney test.

(H) PET-CT images of ^{18}F-FDG uptake by hearts from wild-type and *Mertk*$^{-/-}$ mice. Image quantification is shown in dot plots and given as standard uptake values (SUV) at right. Box and whiskers plot shows data from 10 mice per group. *, $p<0.05$; as determined by unpaired t-test.

STAR Methods

Resources Availability

Lead Contact

Further information and requests for resources and reagents should be directed to, and will be fulfilled by the Lead Contact, Andres Hidalgo (ahidalgo@cnic.es).

Materials Availability

This study did not generate new unique resources, mice or reagents. Further information on materials, datasets, and protocols should be directed to and will be fulfilled by the Lead Contact, Andres Hidalgo (ahidalgo@cnic.es).

Data and code availability

The data referring to the proteomic analyses of Exophers vs Total cardiac tissue and CD169^{DTR} vs Control hearts, have been deposited at PeptideAtlas under accession numbers: PASS01430 and PASS01151, respectively. Any other piece of DATA will be available upon reasonable request.

Experimental Model and Subject Details

Human samples

We obtained papillary muscles from the heart of patients undergoing mitral valve replacement. Inclusion criteria for patients that donated cardiac tissue were age older than 18 years and in need of mitral valve replacement. Emergency procedures were the only exclusion criteria. Five patients were included between July and September 2017. Baseline clinical characteristics of patients are described in Supplemental Table 2. Patients were anesthetized as usual following our local protocol. Median sternotomy and aortic and double venous cannulation were standard. Normothermic bypass was initiated after heparinitation. After antegrade cardioplegia the heart was arrested and left atrial was opened. Mitral valve was excised cutting mitral chordes and the head of papillary muscles. A portion of the papillary muscles head was stored in PFA 4% Glutaraldehyde 1% (for electron microscopy) or PFA 2% (for immunofluorescence), following the protocols described below. This study was conducted in accordance with the Helsinki Declaration and approved by the local ethics committee at Hospital Universitario de la Princesa (Madrid). Written informed consent was obtained from every patient.

Mice

Unless otherwise specified, all experiments were performed in 8- to 18-week-old male mice in a C57BL/6 background. We used heterozygous CX3CR1^{GFP} (Jung et al., 2000), homozygous LysM^{GFP} (Faust et al., 2000) and Csf1r^{GFP} mice (Burnett et al., 2004) as reporters of myeloid cells. Fluorescent protein expression in cardiomyocytes was induced by crossing αMHC^{Cre} (Oka et al., 2006) (referred to as Card^{RED}) or αMHC^{CreERT} (Sohal et al., 2001) with Rosa26^{Tdtom} (Madisen et al.,

2010), or αMHC[Cre] with Rosa26[GFP] (referred to as Card[GREEN] (Sousa et al., 2009)) and in endothelial cells by crossing Cdh5[CreERT] (Sörensen et al., 2009) with Rosa26[Tdtom]. Transgenic mice expressing DsRed under the control of the β-actin promoter (referred to as WT[RED]) (Vintersten et al., 2004), and mice expressing DTR in the *Cd169* locus (CD169[DTR]) (Miyake et al., 2007) were also used. Mice deficient in *Oma1* were generated as described (Quirós et al., 2012). The CD169[DTR]; αMHC[Cre]; Rosa26[Tdtom], and LC3-GFP; αMHC[Cre]; Rosa26[Tdtom] mice were generated by crossing αMHC[Cre] Rosa26[Tdtom] with CD169[DTR] or with LC3-GFP (Mizushima et al., 2004), respectively. Mice deficient in *Mertk* have been previously described (A-Gonzalez et al., 2017). Constitutive or conditional hemizigosity in the *Atg7* gene was achieved by crossing αMHC[Cre] or αMHC[CreERT] with Atg7[flox] mice (Komatsu et al., 2005), respectively. *Atg7*[flox] mice and LC3-GFP mice were kindly provided by Dr. Marco Sandri (University of Padova, Italy) and Dr. Guillermo Mariño (Uiversity of Oviedo, Spain), respectively. Finally, SJL CD45.1 mice from Jackson Laboratory (referred to as CD45.1 or BL/6.SJL[C57]) and a conplastic mouse strain with the nuclear genome of C57BL/6 but mitochondrial DNA of NZB (referred to as BL/6[NZB]) (Latorre-Pellicer et al., 2016) were used. All mice were maintained on a 12h light/12h darkness schedule. Mice were housed in a specific pathogen-free facility at Fundación CNIC. Chow and water were available *ad libitum*. Experimental procedures were approved by the Animal Care and Ethics Committee of the CNIC and local authorities.

Method Details

Animal procedures

Generation of transplanted mice

Recipient WT[RED] (CD45.2) or BL/6.SJL[C57] (CD45.1) mice were lethally irradiated (6.5 Gy split doses, 3 h apart), and subsequently received BL/6.SJL[C57] (CD45.1) or BL/6[NZB] (CD45.2) bone marrow donor cells, respectively. Donor BM cells were harvested by flushing both femora into RPMI and one million were intravenously injected into irradiated recipients.

Parabiosis

To generate parabiotic pairs, we followed our previously described procedures (A-Gonzalez et al., 2017). Anesthetized mice were shaved at the corresponding lateral aspects and matching skin incisions were made from the olecranon to the knee joint of each mouse, and the subcutaneous fascia was bluntly dissected to create about 0.5 cm of free skin. The olecranon and knee joints were attached by a single 5-0 polypropylene suture and tie, and the dorsal and ventral skins were approximated by continuous suture. A single dose of flunixin meglumine (Schering-Plough, Segre, France) was injected subcutaneously in each partner at the end of the surgical procedure (1 mg/kg). One month after surgery blood samples were obtained from each of the partners to assess leukocyte chimerism.

Myocardial infarction

Myocardial infarction was induced by ligation of the proximal left anterior descending (LAD) coronary artery. Mice were anesthetized with a mixture of Atropine, Xylazine and Ketamine and intubated prior to surgery. In order to get access to the heart, a small skin incision was made in

the chest, followed by removal of muscle layers at the level of the third rib. The rib was sectioned and a small orifice was done in the chest, and a knot was made in the LAD coronary artery level using a 8-0 polypropylene suture. For exopher quantification in Card^{RED} mice, LAD was maintained for 7 days without allowing reperfusion. In the case of survival experiments in CD169^{DTR}, LAD was maintained for 45 minutes with mice anesthetized and the knot was removed afterwards. Finally, the incision was closed with 6-0 sutures. After the surgery, a single dose of flunixin meglumine (Schering-Plough, Segre, France) was injected subcutaneously and animals were kept in a 37ºC chamber for the next 24 hours. At day 7 after surgery, animals were sacrificed and cardiac tissue collected.

Hemodynamics

Ventricular catheterization was performed as previously described (Pacher et al., 2008). Mice were anesthetized (ketamine/xylazine (100/10 mg/kg) and intubated. A skin incision was made to visualize the diaphragm, which was heat cauterized to expose the heart apex. The pericardium was removed gently with forceps. Using a 25–30 gauge needle, a stab wound was made near the heart apex into the left ventricle (LV). The catheter tip (Transonic, NY, USA) was inserted retrogradely into the LV. After allowing the signal to stabilize for 5 min, recordings were made of baseline left ventricular end-systolic pressure (LVESP), left ventricular end-diastolic pressure (LVEDP), maximal derivative of LV pressure (dP/dtmax) and minimal derivative of LV pressure (dP/dtmin). The same parameters were recorded 5 minutes after the injection a single dose of isoproterenol (40ng/kg) through the femoral vein when signal was stable. At the conclusion of the experiment, the catheter was removed by gently pulling it back through the stab wound, and the animal was euthanized.

Macrophage depletion

Depletion of cMacs in either CD169^{DTR} or αMHC^{Cre}; Rosa26^{Tdtom}; CD169^{DTR} mice was performed by intraperitoneal injection of 10 μg/kg diphtheria toxin (DT; Sigma). A single injection was administered at the indicated times for transient depletion, or three times a week for long-term (21d) depletion. In these experiments, control wild type or αMHC^{Cre}; Rosa26^{Tdtomato}; CD169^{WT} mice were treated with same doses of DT as the CD169^{DTR} mice. Where indicated, CD169^{DTR} mice treated with saline were used as controls. In control experiments we found that cMacs are the only cardiac cells targeted by, and depleted in the CD169^{DTR} model (not shown) and that depletion of these cells, while depleting macrophages from other organs (Casanova-Acebes et al., 2018), does not cause systemic or local inflammation (Supplemmentary Table 1).

Induction of Cre recombinase with Tamoxifen

We use several Inducible Cre strains. Fluorescent protein expression in endothelial cells was induced in Cdh5^{CreERT} Rosa26^{Tdtom} mice by intraperitoneal treatment with tamoxifen (1mg/mice) at days 11, 9 and 7 before analysis. In order to obtain mosaics of Tdtomato+ cardiomyocytes in αMHC^{CreERT} Rosa26^{Tdtom} mice, we gave a single dose of tamoxifen at 1μg/mice. Finally, conditional deficiency in *Atg7* on cardiomyocytes of αMHC^{CreERT} Atg7^{flox} mice was induced by injecting tamoxifen (1mg/mice) for two consecutive days.

Treatment with rapamycin and isoproterenol

For some experiments, animals were treated trice per week with Rapamycin (4mg/kg body weight; LC Laboratories) intraperitoneally for 2 weeks and analyzed at day 14. Isoproterenol hydrochloride (ISO; 25 mg/kg/day; Sigma-Aldrich) was chronically administered in mice in minipumps. Mice were anesthetized with Sevoflurane (2.5-3.5 % and 1 % O_2) and osmotic minipumps (Mini-Osmotic Pump, Alzet) were subcutaneously implanted for continuous delivery during 7 consecutive days. Finally, for some experiments animals were administrated daily with MCC950 (intraperitoneal, 7 mg/kg/day) or ISO (subcutaneous, 50mg/kg/day) for the indicated times.

Experimental setups

Identification of phagocytic macrophages

Preparation of cMacs from digested hearts was performed as indicated above. Phagocytic cMacs were identified based on the incorporation of DsRed or tdTomato fluorescence, as shown in Fig.S2B-C. Engulfment of material in CD45.1-WT[RED] bone marrow chimeras was based on acquisition of DsRed signal by CD45.1-derived cardiac macrophages in WT[RED] transplanted mice. Engulfment of cells in parabionts of CD45.1 with WT[RED] mice was based on acquisition of DsRed signal by tissue-resident macrophages in the non-fluorescent partner as previously described (A-Gonzalez et al., 2017). Non-parabiotic CD45.1 mice were used as controls to set the appropriate gates. Engulfment of cardiomyocyte- and endothelial cell-derived material in αMHC[Cre]; Rosa26[Tdtom] and Cdh5[CreERT]; Rosa26[Tdtom], respectively, was based on tdTomato signal acquisition by cMacs when comparing with non-fluorescent control mice.

Generation of adeno-associated virus and transduction of the mt-Keima reporter.

AAV vectors were all produced by the triple transfection method, using HEK 293A cells as described previously (Xiao et al., 1998). Shuttle plasmid pAAV-mt-Keima was derived from mt-Keima-Red-Mito-7 (a gift from Michael Davidson (Addgene plasmid #56018)) and from pAcTnT (a gift from B.A. French). The mt-Keima cDNA is a fusion of *Keima* gene in-frame to the matrix import sequence of human Cox8A: MSVLTPLLLRGLTGSARRLPVPRAKIHSLPPEGKLGM. The expression is driven by the cardiac-specific promoter *TnT* (see Fig.S3B).Virus were packaged into AAV-9 capsids by the CNIC Viral Vector Unit using helper plasmids pAdDF6 (providing the three adenoviral helper genes) and pAAV2/9 (providing rep and cap viral genes). Four- to 6-week-old mice were injected with 3-10 x 10^{10} viral genomes encoding mt-Keima and analyzed 2 to 6 weeks later. We confirmed no expression of mt-keima in cMac isolated from AVV9-mt-keima infected mice (Fig.S3C). To control for no leaky expression of Tnnt2-mt-Keima in macrophages, we transfected the RAW264.7 macrophage or HL1 cardiomyocytic cell lines with a *Tnnt2*-mt-keima (driven by the cTnT promoter) or Cmv-mt-Keima (driven by a CMV promoter) constructs, plus a transfection control (cmv-GFP). RAW264.7 failed to express mt-Keima under the TnnT2, but not the CVM promoter, whereas HL1 cells expressed both (data not shown).

Detection of exogenous mitochondrial DNA in macrophages

BL/6.SJL[C57] mice (with C57BL/6 nuclear and C57 mitochondrial DNA) were lethally irradiated and transplanted with BL/6[NZB] bone marrow (C57BL/6 nuclear and NZB mitochondrial DNA), as described above. Differential expression of the CD45.1/CD45.2 surface marker on these strains additionally allowed cytometric discrimination and sorting. Macrophages from CD45.2+ BL/6[NZB] donors were isolated from different tissues by cytometric sorting and DNA isolated using NaOH

50mM at 95ºC, and neutralization with TrisHCl pH 7.5. A polymorphic G4276A nucleotide in the mitochondrial ND2 gene was used to discriminate the mtDNA source in the samples. This polymorphism in C57 mtDNA forms part of a BamHI restriction site, which is absent in NZB mtDNA (Latorre-Pellicer et al., 2016). Total genomic DNA was PCR amplified using standard conditions with the REDExtract-N-Amp™ PCR ReadyMix™ and the primers used were Fw(5´>3´)AAGCTATCGGGCCCATACCCCG; Rv(5´>3´)GTTGAGTAGAGTGAGGGATGGG. An aliquot of PCR was digested with FastDigest BamHI (New England Biolabs), at 37ºC for 10-15 minutes. After agarose gel electrophoresis, DNA was visualized with a Gel Doc XR+System (Bio-Rad), and band intensities were quantified with Quantity One 1-D Analysis Software. The proportion of C57 mtDNA was calculated by adding the intensities of the 414bp and 250bp BamHI fragments and dividing by the sum of the intensities of all fragments (undigested 664bp fragment from NZB mtDNA, and the 414bp and 250bp BamHI-digested fragments from C57mtDNA).

Degradation of exogenous mtDNA and mt-Keima in cMacs

We sorted cMacs from mt-Keima-infected hearts or from BL/6[NZB]-transplanted BL/6.SJL[C57] and cultured a maximum of 3×10^5 cardiac macrophages per well in 48w plates. We used a medium with αMEM containing Na-Pyruvate, L-Glutamine and Penicillin/Streptomycin, plus Essential aminoacids, including 10% FBS and 10 ng/mL M-CSF. Macrophages were cultured for 72h at 37Cº, 5% CO2.

Flow cytometry and cell sorting

Tissue preparation, flow cytometry and cell sorting

The large intestine (colon) was cut into small pieces and subjected to epithelial separation by incubation with HBSS with 2mM of EDTA for 20 min at 37ºC and subsequently digested in HBSS with liberase (1U/ml, Roche) and DNase I (10 mU/ml, Sigma) for 40 min at 37°C. Bone marrow was flushed and hearts, skeletal muscle, livers, and spleens were minced and digested in HBSS with liberase (1U/ml, Roche) and DNase I (10 mU/ml, Sigma) for 30min at 37ºC. After digestion, single-cell suspensions were obtained by gentle pipetting and mechanical dissociation of the remaining pieces through cell strainers (BD Falcon). Single-cell suspensions were incubated with conjugated antibodies against CD45 (clone 30-F11), CD45.1 (clone A20), CD45.2 (clone 104), CD11b (clone M1/70), F4/80 (clone BM8), MHCII (clone M5/114.15.2), Ly6C (clone HK1.4), CD115 (clone AFS98) and Gr1 (RB6-8C5) for 15 min at 4°C (see Key Resources table for further information). Samples were acquired in a LSRII Fortessa (BD Biosciences) or Canto HTS (BD) equipped with DIVA software (BD). The FlowJo software (FlowJo LLC, Ashland, OR) was used to analyse the data.

Estimation of absolute numbers of cells per tissue using fluorescent beads

Truecount beads (BD) were prepared at a concentration of 10,000 beads per ml in a buffer containing EDTA 0.5M, FBS 0.5% (PEB) and 0.1 µg/mL DAPI (Life Technologies) in PBS. 500 µl of this PEB/DAPI buffer containing beads were added to single cell suspensions stained for flow cytometry as indicated above. To estimate the absolute number of cells, 500-1000 beads were acquired per tube in order to ensure accuracy. Cell counts per mg of tissue were calculated as follows:

$$\frac{cells}{beads} \; x \; \frac{10,000 \; beads}{ml \; PEB \; buffer} \; x \; \frac{0,5 \; ml \; PEB \; buffer}{fraction \; of \; tissue \; digested} \; x \; \frac{1}{weight \; of \; organ \; (mg)} = \frac{cells}{mg}$$

For blood, absolute cell numbers given as cells per ml were obtained using an automated hemocounter (Abacus Junior, Diatron; Holliston, USA).

Preparation of cardiac exophers for flow cytometry and sorting

The heart of Card^{RED} mice was cut into small pieces and subsequently digested in HBSS with liberase (1U/ml, Roche) and DNase I (10 mU/ml, Sigma) for 40 min at 37°C. After digestion, single-cell suspensions were obtained by gentle pipetting. We used a strategy of serial centrifugation forces (see Fig.S2K) at 50g and 300g discarding pellet and keeping supernatant for a final centrifugation at 1000g. Within the pellet of this fraction, we used the endogenous expression of tdTomato along with size, antibody (CD31-Bv605; clone 390 Biolegend) and Draq5 staining (Biolegend) to define cardiac exophers. The material was sorted in an Aria Cell Sorter (BD) equipped with DIVA software (BD). In some experiments, exophers were stained for Mitotracker Deep Red (ThermoFisher), MitoNIR (Abcam). This protocol is an adaptation of previously described protocols to obtain samples enriched in apoptotic bodies (Atkin-Smith et al., 2017). Part of the material obtained in each fraction was subjected to cytospin in a Shandon Cytospin™ 4 Cytocentrifuge (ThermoFisher) at 1000 rpm for 5 minutes at medium velocity. Cells and exophers were then fixed in 4% paraformaldehyde for 5 min, permeabilised with 0.01% TritonX100 in PBS for 15 minutes and blocked 1 hour with 10% BSA and 2% goat serum. For immunofluorescence analysis, samples were incubated with rabbit anti-RFP (polyclonal; Rockland), washed thrice in PBS and incubated with secondary antibodies (Goat anti-Rabbit AF546; Molecular Probes).

Analysis of mitochondrial membrane potential by flow cytometry

Oligomycin (10 mg/ml; Sigma-Aldrich) was used to promote mitochondrial hyperpolarization (ATP synthase inhibition). Carbonyl cyanide-4 (trifluoromethoxy) phenylhydrazone (FCCP, 1uM) uncouples oxygen consumption, collapses the proton gradient and ablates the mitochondrial membrane potential. Total cardiac leukocyte fraction and cardiac purified exopheres were treated for 3 hours at 37ºC. Inmortalized mouse adult fibroblasts (MAFs) were used as internal control to assess treatment responsiveness. Mitochondrial membrane potential was measured by using the fluorescent probe MitoNIR (Abcam) by flow cytometry as per the manufacturer's instructions. Cells were incubated in culture medium supplemented with 1x MitoNIR for 20 minutes at 37ºC. Data acquisition was performed using the FACSCanto™ II system (BD Biosciences). All experiments were performed in triplicates. Samples were analyzed with the BD FACSDiva™ software package and the average of the medians and corresponding standard deviations were calculated using the FlowJo software (v10).

Imaging Techniques

Light-sheet microcopy of whole hearts and estimation of macrophage numbers

4 week-old heterozygous CX3CR1^{GFP} mice were euthanized and immediately transcardially perfused with 10ml PBS containing 2mM EDTA pH7.4, followed by 10ml of 4% paraformaldehyde (PFA) through the left ventricle. The heart was dissected and fixed in 4% PFA (Sigma) overnight at 4°C, followed by extensive washing with PBS. The fixed hearts were permeabilised with graded methanol solutions from 50%, 70%, 95% and 100%, each incubated for 45minutes, followed by

100% methanol/20%DMSO for 1 hour. Tissue was rehydrated back to PBS with 45 minute incubation at room temperature. Permeabilised sample was blocked overnight in blocking buffer (2.5% goat serum, 2.5% donkey serum, 5% BSA, 0.02% gelatin, 20%DMSO, 0.3% TritonX100 in PBS), washed extensively with PBS and incubated with primary antibodies in dilution buffer (2.5% goat serum, 2.5% donkey serum, 0.2% BSA, 0.02% gelatin, 5%DMSO, 0.3% TritonX100 in PBS) for 48 hours. Chicken anti-GFP (1:300 dilution, Abcam polyclonal) and Armenian hamster anti-CD31 antibodies (1:300 dilution; clone 2H8, Merck) were used. Samples were washed 6 times with 3M NaCl+0.3% TritonX100 in PBS, and twice with PBS. Each wash was for 30minutes at room temperature. Tissues were incubated with secondary antibodies (anti-chicken Alexa fluor-647, anti-hamster Alexa fluor-750; Abcam) at 1:300 in dilution buffer for 48 hours, washed as indicated above and taken for tissue clearing. All antibody incubations were carried out at 37°C. Heart tissue was cleared using the BABB (Benzyl alcohol/ Benzyl benzoate) protocol. Samples were dehydrated with methanol as for permeabilization, equilibrated with BABB:methanol in a 1:1 ratio for 45 minutes and the refractive index matched with BABB (1:2) for 45 minutes until clear. Cleared hearts were imaged using the light sheet Ultramicroscope (LaVision BioTec GmbH, Bielefeld, Germany) in BABB with a 2X objective, NA 0.5, using a white light supercontinuum laser. Post-acquisition, high resolution raw data was downsampled and corrected to remove high intensity artifacts arising from uneven light illumination during acquisition, using Imaris 8.0 (Bitplane AG). Image contrast was further improved using the unsharp mask function of FIJI Is Just ImageJ (NIH), and rendered in 3D using Imaris 8.0. Macrophage number in the whole organ was quantified using GFP signal in Cx3cr1^{GFP} mice for segmentation with surface tool in Imaris 8.0.

Immunofluorescence of cardiac tissue

Mice were sacrificed with CO_2 and perfused with a saline solution in order to collect the hearts into a 2% PFA solution. Human samples for immunofluorescence fixed in PFA 2% were obtained as indicated above. After 24 hours in fixation solution at 4ºC, samples were cryopreserved with a sucrose gradient, and frozen in OCT Compound (Tissue Tek) using dry ice. Tissues were cut in 12µm (most of them) or 30µm (for 3D reconstructions) sections in a cryostat (Leica CM1850). Macrophage detection by immunofluorescence was carried out in cardiac slices permeabilised with 0.01% TritonX100 in PBS for 15 minutes and blocked 1 hour with 10% BSA and 2% goat serum. For immunofluorescence, mouse tissues were incubated with rat anti-CD68 (clone FA-11; BioRad), rat anti-CD169 (clone 3D6; kindly provided by S.Gordon), rabbit anti-laminin (polyclonal; Sigma), rabbit anti-NDUFS2 (Polyclonal Abcam), rabbit anti-Cytochrome C (clone EPR1327; Abcam), rabbit anti-Tom20 (clone FL-145; Santa Cruz Biotechnology), rabbit anti-Myh7 (clone NOQ7.5.4D; Sigma), rabbit anti-Optineurin (clone EPR20654 Abcam), rabbit anti-PEX14 (polyclonal Proteintech), rabitt anti-GM130 (clone EP892Y Abcam), mouse anti-keima (clone 1C3 MBL), chicken anti-GFP (polyclonal invitrogen) or rabbit anti-LAMP1 (polyclonal; Sigma) primary antibodies. Humans samples were incubated with mouse antibodies anti-CD68 (clone PG-M1; Dako), mouse anti-MYH (clone MF20; DSHB) or rabbit anti-Tom20 (clone FL-145; Santa Cruz Biotechnology). Tissues were washed thrice in PBS and incubated with secondary antibodies (Molecular Probes) or Phalloidin-AF647 (Thermofisher). All staining steps were conducted in blocking solution for 1 hour at room temperature. Finally, tissues were washed in PBS and nuclei were counterstained with DAPI (Life Technologies) before mounting with Mowiol 4–88 (Sigma-Aldrich).

Phosphatidyl-serine (PS) staining in live heart sections and exophers FACS preparations.

Hearts from heterozygous CX3CR1^{GFP} mice were collected in excision buffer (HBSS 1x, FBS 5% at pH7.4) and manually cut perpendicular to the ventricular walls to form 1-2 mm thick rings of tissue. Those slices were incubated with Annexin V-PE (BD Biosciences) in Annexin binding buffer (10mM HEPES/NaOH, pH 7.4; 140 mM NaCl; 2,5 mM CaCl2) with or without EDTA 1mM as control, since Annexin-V binding to PS is calcium dependent. For imaging, slices were placed into glass petri plates containing fresh Annexin binding buffer and immobilized with a coverslip. Images were taken in an SP5 microscope (Leica) maintaining 37 ºC and 5% O2 levels. Tissue borders were avoided to exclude areas of dead cardiomyocytes. We measured the distances between macrophages and phosphatidylserine (Annexin V+) patches using FIJI Is Just ImageJ (NIH), and compared them to the same number of random spots in those images. Random spots were 1 µm diameter circles (similar to the phosphatidylserine patches) generated by a macro using FIJI Is Just ImageJ (NIH). For FACS, we incubated exophers preparations from Card^{RED} mice (as in Fig.S2K) with Annexin V-APC (BD Biosciences) in Annexin binding buffer for 15 minutes before analysis.

Co-culture experiments

Cardiac macrophages were isolated from hearts of DsRed transgenic mice by FACS sorting using an Aria Cell Sorter (BD) equipped with DIVA software (BD). We co-cultured these DsRed+ macrophages with HL1^{GFP} cells for 18 hours in an 8-well IBIDI plate and performed imaging for 2 hours in a Nikon Time Lapse microscope at 37ºC and 5% CO$_2$. After imaging, cells were fixed with PFA 2% for 15 min for immunostaining with Rabbit anti-Tom20 antibody (clone FL-145; Santa Cruz Biotechnology) and Secondary Goat Anti-Rabbit antibody (Molecular Probes).

Transmission Electron Microscopy (TEM).

For TEM analysis of WT, CD169^{DTR} and *Mertk*$^{-/-}$ mice or human samples, heart pieces were first fixed in 1% glutaraldehyde and 4% PFA in PBS, overnight at 4ºC. Samples were post fixed in 1% osmium tetroxide for 60 minutes and dehydrated through a series of ethanol solutions (30%, 50%, 70%, 95%, and 100%) and acetone. After the last dehydration step, samples were incubated in a 1:3, 1:1, 3:1 mixture of Durcupan resin and acetone and cured at 60º for 48h. Ultrathin sections (50-60 nm) were obtained using a diamond knife (Diatome) in an ultramicrotome (Leica Reichert ultracut S) and collected in 200-mesh copper grids. The sections were counterstained with 2% uranyl acetate in water from 20 min followed by a lead citrate solution. Samples were examined with a JEOL JEM1010 electron microscope (Tokyo, Japan) equipped with an Orius SC200 digital camera (Gatan Inc.) at the Transmission Electron Microscopy Laboratory (Interdepartmental Research Service, UAM). For images of isoproterenol-treated mice, tissue samples were processed as previously described (Latorre-Pellicer et al., 2016).

Echocardiography.

Echocardiography assessment was blinded and performed by an expert operator in mice under isoflurane anesthesia using a high-frequency ultrasound system with a 30-MHz linear probe (Vevo 2100, Visualsonics Inc., Canada). A base apex electrocardiogram was continuously monitored through 4 leads connected to the ultrasound machine and isoflurane delivery was adjusted to maintain the heart rate in 450±50 bpm. Normothermia was maintained placing mice in a heating platform. Images were recorded and transferred to a computer for posterior blinded analysis using the Vevo 2100 Workstation software. Parasternal standard 2D and MM long axis view were

acquired to assess left ventricle (LV) systolic function and LV dimensions. LV ejection fraction (LV-EF), end-diastolic and end-systolic LV volume (LV-Vol,d and LV-Vol,s; respectively) and Cardiac Output were subsequently calculated. A 2D apical view was used to evaluate diastolic dysfunction, using pulsed-wave (PW) Doppler, to estimate mitral valve inflow pattern. Early and late diastolic velocity peak waves (E and A, respectively) were measured and the E/A ratio calculated.

Image Analysis

Quantification and localization of cardiac exophers by inmmunofluorescence

Quantification and localization of cardiac exophers relative to CD68, CytC, Ndufs2, Tom20, MYH7 and DAPI was done manually, as the Tomato signal from Card^{RED} cardiomyocytes did not allow segmentation. The criteria for co-localization was overlapping positions of tdTomato signal in exophers of αMHC^{Cre}; Rosa26^{Tdtom} mice and the stained markers, while the percentage of co-localization between cardiac exophers and any other "marker" was quantified as follows:

$$\% \text{ of exophers co} - \text{localizing with "marker"} = \frac{\text{N. of exopheres colocalizing with "marker" x 100}}{\text{N. of total exopheres}}$$

We measured the distances between macrophages and cardiac exophers using FIJI and ImageJ softwares (NIH), and compared these distances to the same number of random spots in those images. Random spots were 3.5 µm diameter circles (similar to cardiac exophers) generated by a macro using FIJI Is Just ImageJ (NIH).

Analysis of 3D reconstructions of cardiomyocyte exophers.

We measured the 3D features of cardiac exophers and cardiac macrophages using Imaris Software (Bitplane AG, Switzerland). For 3D reconstructions, we used 0.25 µm detail level and a threshold based on absolute intensity. The source channels for the reconstruction of cardiac exopheres and cardiac macrophages were tdTomato in αMHC^{Cre} Rosa26^{Tdtom} mice and CD68-FITC, respectively. From the parameters provided by the ImarisCell module we selected Volume, Area and Sphericity. In the case of cardiac exophers, diameter was calculated from Volume considering them as perfect spheres due to their high Sphericity index (0.71±0.01 in exophers vs. 0.37±0.01 in cMacs).

Visualization and quantification of cMacs-to-cardiomyocyte ratios

The cMac to cardiomyocytes ratios were analyzed in CX3CR1$^{GFP/+}$ mice. Hearts from these mice were fixed and frozen as described in the immunostaining method. We obtained thick slices (60 µm) from OCT-included samples using a cryostat and subjected them to permeabilization (in PBS + Triton 0.1% solution), blocking (10% BSA, 5% NGS in PBS) and staining steps, all of them performed overnight at 4ºC. We stained the samples with primary rabbit anti-laminin (polyclonal; Sigma) and secondary goat anti-rabbit AF546 antibodies to label the cardiomyocyte basal lamina. We performed quantification of cMacs and cardiomyocytes spatial interactions in 30 µm thick optic fields obtained using an SPE microscope (Leica). For the visualization of individual cardiomyocytes we used tissues of αMHC^{CreERT}; Rosa26^{Tdtom} mice. Cardiac tissue was fixed in a 2% PFA solution. After 24 hours in fixation solution at 4ºC, samples were incubated thrice with washing buffer (0.05%

tritonX-100 in PBS) for one hour each and blocked with 1% BSA in PBS overnight. For immunofluorescence, mouse tissues were incubated with rat anti-CD68 (clone FA-11; BioRad) and rabbit anti-RFP (polyclonal; Rockland) primary antibodies and goat secondary antibodies (Molecular Probes). After immunostaining, tissues were washed thrice with washing buffer (0.05% tritonX-100 in PBS) for one hour each and dehydrated with an ethanol gradient (50%/70%/100% twice) before inclusion in clearing solution (Ethyl cinnamate; Sigma). A large portion of the tissue was imaged using a SP8 microscope (Leica) equipped with a resonant scanner, and then reconstructed using Imaris 8.0 (Bitplane AG).

Evaluation of phagolysosomal content using Keima fluorescence

Keima is a fluorescent protein resistant to lysosomal proteases, with an emission spectrum that peaks at 620 nm and a bimodal excitation spectrum peaking at 440 and 586 nm corresponding to the neutral and ionized states of the chromophore's phenolic hydroxyl moiety, respectively (Violot et al., 2009). Neutral and ionized states predominate at high and low pH, respectively, thus allowing measurement of mitophagy in vitro and in vivo (Katayama et al., 2011; Sun et al., 2015). We used this property to evaluate mitochondria degradation in macrophages by measuring ratiometric "red-to-green" fluorescence intensities in Keima+ regions co-localizing with macrophages (CD68+) or cardiomyocytes. Imaging was done using an SP5 confocal microscope (Leica) in two channels via two sequential excitations (458 nm for "green"; and 561 nm for "red" excitation), and a 590–650 nm emission filter in both cases. Laser power was set at the lowest output that would allow clear visualization of the mt-Keima signal. CD68 labelling (for macrophages) was detected using a 488 nm excitation and a 510–550 nm emission filter.

Sarcomere and mitochondrial morphology

Cardiomyocytes area, perimeter and shape descriptors where measured by manually definition of cardiomyocytes borders in images from cardiac sections (using laminin staining) and isolated cardiomyocytes (bright field) using ImageJ. Sarcomere length and mitochondria size and shape were obtained by visual inspection and segmentation of these structures in transmission electron microscopy (TEM) images, using ImageJ.

Hematoxylin / Eosin staining

Cardiac macrophages were isolated by FACS and subjected to cytospin in a Shandon Cytospin™ 4 Cytocentrifuge (ThermoFisher) at 800 rpm for 5 minutes, at medium velocity. Cells were then fixed in 4% paraformaldehyde for 5 min, stained in eosin for 5 min, washed in dH$_2$O, stained in hematoxilin for 5 min, and finally washed and mounted with dH$_2$O.

Mitochondrial function and autophagy flux

Mitochondria Isolation and OXPHOS function

Mitochondria were isolated from mouse heart and liver samples as described (Lapuente-Brun et al., 2013) and ATP synthesis was measured by kinetic luminescence assay (Vives-Bauza et al., 2007). Mitochondria were resuspended in 160 µl buffer A (150mM KCl, 25mM Tris-HCl, 2mM EDTA, 0.1% BSA FA, 10mM K-phosphate and 0.1mM MgCl$_2$, pH 7.4) at room temperature and dispensed into the wells of a 96-well luminescence reading plate (Costar). Substrate cocktail and

buffer B (0.5M Tris-acetate pH 7.75, 0.8mM luciferine, 20 μg/ml luciferase) were added, and luminescence was measured over 1 min. Substrate cocktails were composed of 6 mM diadenosin pentaphosphate and 6 mM ADP supplemented with glutamate + malate for determination of CI activity, or with succinate for CII activity or palmitate + carnitine for assessment of fatty acid oxidation. The ATP production rates were normalize to citrate synthase activity (see below) and expressed as the amount of ATP produced (nmol / min / mg of protein) relative to controls. Technical duplicates were performed and the average value for each animal was represented. Cytrate synthase activity was determined spectrophotometrically as described (Birch-Machin and Turnbull, 2001). 5-10 μg of total protein from tissue homogenates or isolated exophers were used for the assay. Investigators were not blinded to the group allocation.

$^{31}P/^1H$ Magnetic resonance spectroscopy ($^{31}P/^1H$-MRS)

Mice were anesthetized with isoflurane during the whole acquisition. Spectroscopy examinations were performed in vivo on a 7T preclinical system (Agilent Varian, Palo Alto, USA) equipped with a DD2 console and an active shielded 115/60 gradient insert coil with 433 mT/m maximum strength. Double-tuned circular transmit/receive coil were used for phosphorus/proton (20 mm), placed over cardiac muscle (Rapid Biomedical GmBH, Rimpar Germany). Proton tissue spectra were acquired by 128 transients with 2048 complex points with a spectral bandwidth of 10 kHz and a repetition time of 1.2 ms. Phosphorus tissue spectra were acquired by 1000 transients with 8192 complex points with a spectral bandwidth of 7 kHz and a repetition time of 800ms. Spectra were acquired with adiabatic radiofrequency pulses to improve sensitivity and minimize spectral distortions with an Ernst flip angle. Chemical shift were expressed relative to phosphocreatine (0 ppm). Signals in nuclear magnetic resonance spectra were determined quantitatively by integration after automatic or manual baseline correction, with fitting of each peak of the spectrum (after phase and baseline correction) to a Lorentzian function using the Mestrenova program (Mestrelab Research, Santiago de Compostela, Spain; released 2015-02-04 version:10.0.1-14719). An exponential line broadening (3 Hz for proton) was applied before Fourier transformation.

^{18}F-FDG uptake by Positron emission tomography (PET) - computed tomography (CT)

All acquisitions were performed with a small-animal PET/CT scanner (nanoScan, Mediso). PET studies were acquired 30 minutes after intravenous administration of 17 MBq of ^{18}F-FDG. During FDG uptake, the animals were kept awake and warm to prevent brown fat uptake. PET data were then collected for 30 minutes with the mice anesthetized using 1.5% sevoflurane in oxygen at 3 L/min and reconstructed using Tera-Tomo 3D with 6 subsets, 4 iterations, an energy window of 400-600 keV and a coincidence mode of 1-5. The voxel size of the reconstructed images was 0.399 mm in the transaxial plane and 0.399 mm in the axial plane. After the PET scan, a helicoidal CT study was acquired using an X-ray beam exposure of 89 μAs and a tube voltage of 45 kVp and reconstructed using a Ramlack algorithm. These CT scans were used as anatomical templates. PET values were measured as standardized uptake value (SUV) over the segmented region corresponding to the left ventricle. On the PET images, the regions of interest were delimited over the whole hearts to measure their corresponding SUV (SUV mean).

Autophagy flux analysis

Animals were euthanized and the heart was quickly removed, cannulated through the ascending aorta, and mounted on a Langendorff perfusion apparatus. The heart was then retrogradely perfused for 4 min at room temperature (RT) with pre-filtered Ca2+-free Perfusion-Buffer [NaCl (113 mmol/L); KCl (4.7 mmol/L); KH2PO4 (0.6 mmol/L); Na2HPO4 (0.6 mmol/L); MgSO4·7H2O (1.2 mmol/L); NaHCO3 (12 mmol/L); KHCO3 (10 mmol/L); HEPES (10 mmol/L); taurine (30 mmol/L); glucose (5.5 mmol/L); 2,3-butanedione-monoxime (10 mmol/L), pH 7.4]. Enzymatic digestion was performed with digestion-buffer consisting in perfusion-buffer with Liberase™ (0.2 mg/mL), Trypsin 2.5 % (0,14 mg/mL); CaCl2 (12.5 µmol/L) and Phenol Red (0.032 mmol/L)] for 20 min at 37 °C. At the end of enzymatic digestion, both ventricles were isolated and gently disaggregated in 5 mL of Digestion Buffer. The resulting cell suspension was filtered through a 100-µm sterile mesh (SEFAR-Nitex) and transferred for enzymatic inactivation to a tube with 10 mL of stopping-buffer-1, which consisted in perfusion-buffer supplemented with fetal bovine serum (FBS, 10 % v/v) and CaCl2 (12.5 µmol/L). After gravity sedimentation for 15 min, cardiomyocytes were resuspended in stopping-buffer-2 containing 5% FBS (v/v) for 10 min. Cardiomyocyte Ca2+-reintroduction was performed in stopping-buffer-2 with two progressively increased $CaCl_2$ concentrations (112 µmol/L and 1 mmol/L). Cells were resuspended and allowed to decant for 10 min in each step, allowing purification of the cardiomyocyte suspension. Homogeneous suspension of rod-shaped cardiomyocytes was then resuspended in M199 supplemented with l-glutamine, pyruvate, penicillin–streptomycin (1 %), bovine serum albumin (BSA, 2 g/L), blebbistatin (25 µmol/L) and FBS (5 %). Cells were plated in single drops onto 20-mm^2 glass bottom microwell dishes (MatTek) precoated with 100 µL of mouse laminin (200 µg/mL) in 900 µL NaCl 0.9% for at least 1 h. For each mouse, 2 dishes were used as a control culture and 2 dishes were treated with Hydroxycloroquine (30 µM) for 12h to block lysosomal degradation. After culture, cardiomyocytes were fixed overnight at 4°C in 2% paraformaldehyde in PBS. After fixation, immunofluorescence was made following standard procedures: fixation in methanol at 4ºC for 10 min, permeabilized with 0.5% Triton-X 100 and blocked in PBS containing 10% goat serum and 0.1% Triton-X 100. Anti-LC3 antibody (clone 5F10 Nanotools) primary antibody was used and Nuclei were co-stained with DAPI. Isolated cardiomyocytes were then imaged with a Leica SP5 confocal microscope using 20×/0.75 dry and 63×/1.30 oil objectives. Quantifications were made by using the macro plugin tool in image J, which automatically detected individual cardiomyocytes and quantified the number of LC3, dots per cell. Autophagy was determined by evaluating autophagic flux that is achieved by comparing the number of LC3-positive autophagosomes in the absence and presence of lysosomal inhibitors like hydroxychloroquine.

Molecular analyses

Western blot analyses

Total heart protein homogenates were separated by 12.5% SDS polyacrylamide gel electrophoresis (SDS PAGE) and electro blotted onto PVDF transfer membrane (BioRad). For protein detection, the following antibodies were used: NLRP3 (clone 25N10E9; ThermoFisher), Caspase-1 (clone 14F468; Santa Cruz), LC3 (Polyclonal; Cell Signal) and p62 (polyclonal; Cell Signal). Western blot images were quantified by using ImageJ software (National Institutes of Health, Bethesda) and Ponceau S staining was selected as a loading control.

Detection of molecular markers of Tissue damage in plasma

Blood was collected using EDTA tubes and then centrifuged 15 minutes at 4ºC at 2000 x g to isolate plasma. The biochemical profile was assessed with a Dimension RxL Max®automated analyser. All reagents used for the analyses in Fig.S6E and Supplementary Table 1 were purchased from Siemens.

Proteomic analysis of cardiac tissue

For proteomic studies in wild-type and CD169[DTR] mice after depletion, hearts were collected from PBS perfused animals and frozen in liquid nitrogen.Protein extracts were obtained by tissue homogenization with ceramic beads (MagNa Lyser Green Beads, Roche, Germany) in extraction buffer (50 mM Tris-HCl, 1 mM EDTA, 2% SDS, pH 8.5 – 8.8, 50 mM DTT). The protein extract for each time-point from three biological replicates, and an internal standard generated as a pool of peptides from all biological conditions, were subjected to tryptic digestion and the resulting peptides were labelled with 10-plex isobaric mass tags for relative quantification (TMT, Thermo Scientific). Labelled peptides were subjected to peptide separation into different fractions using a Waters Oasis MCX cartridge (Waters Corp, Milford, MA) or high pH reversed-phase peptide fractionation kit (Thermo Fisher Scientific). The fractionated peptides were then analyzed by nano-liquid chromatography-tandem mass spectrometry (nanoLC-MS/MS) using a Q-Exactive mass spectrometer (Termo Scientific). Protein identification was performed using the SEQUEST HT algorithm integrated in Proteome Discoverer 1.4 (Thermo Scientific). MS/MS scans were searched against a mouse reference proteome database (UniProtKB/Swiss-Prot 02_12_2015). Peptides were identified from MS/MS data using the probability ratio method (Martínez-Bartolomé et al., 2008) and the False discovery rate (FDR) of peptide identifications was calculated by the refined method (Bonzon-Kulichenko et al., 2015). Quantitative information was extracted from the MS/MS spectra of TMT-labeled peptides using a SQL query from the Thermo Proteome Discoverer file (.msf). Protein abundance changes were expressed as log2-ratios in standardized units z_q (Navarro et al., 2014). Significant protein abundance changes for the indicated contrasts were defined by applying Student's t-test to z_q data, and differences were considered statistically significant at $p<0.05$. The differentially expressed proteins were then analysed using Ingenuity Pathway Analysis (IPA, Quiagen, http://www.ingenuity.com). Pathways with adjusted p-values below 0.05 were considered overrepresented and shown as Bubble plots.

Proteomic analysis of cardiac exophers versus Total cardiac tissue

We used hearts form Card[RED] mice and exophers isolated from the same mice as indicated in Fig.S2K and the Methods section. Mice were perfused with PBS and approximately 50 mg of tissue was frozen in liquid nitrogen from each heart, while the rest was used to isolate the corresponding exospheres. The protein extracts were obtained in extraction buffer (50 mM Tris-HCl, 1 mM EDTA, 2% SDS, pH 8.5 – 8.8, 50 mM DTT) by tissue homogenization with ceramic beads (MagNa Lyser Green Beads, Roche, Germany) for total hearts and by heating (5 min at 90ºC), vortexing and centrifugation (10 min at 16100g) for cardiac exophers. Protein lysates from the exospheres and the corresponding heart tissue were boiled in 2x Laemmli sample buffer, subjected to in-gel digestion (Bonzon-Kulichenko et al., 2011) and analyzed using a Proxeon Easy nano-flow HPLC system (Thermo Fisher Scientific, Bremen, Germany) coupled via a nanoelectrospray ion source (Thermo Fisher Scientific) to an Orbitrap Fusion mass spectrometer (Thermo Fisher). C18-based reverse phase separation was used with a 2-cm trap column and a 50-cm analytical column (75 µm I.D, 2 µm particle size, Acclaim PepMap RSLC, 100 C18; Thermo Fisher Scientific) in a

continuous acetonitrile gradient consisting of 0-30% A for 120 min, 50-90% B for 3 min (A= 0.1% formic acid; B= 90% acetonitrile, 0.1% formic acid) at a flow rate of 200 nL/min. Mass spectra were acquired in a data-dependent manner, with an automatic switch between MS and MS/MS using a top 15 method and dynamic exclusion. MS spectra in the Orbitrap analyzer were in a mass range of 400–1500 m/z and 120,000 resolution. HCD fragmentation was performed at 33 eV of normalized collision energy and MS/MS spectra were analyzed at 30,000 resolution in the Orbitrap. Protein identification was performed as described above (Proteome Discoverer 2.1; Thermo Scientific) and MS/MS scans were searched against a mouse reference proteome database (UniProtKB/Swiss-Prot April_2018), supplemented with the tdTomato and 116 CRAP proteins (Global Proteome Machine) (16988 sequences in total). Peptide identification from MS/MS data was performed as described above. In order to obtain maximum reliability, we eliminated from the analysis all proteins that had less than 6 counts among all samples, and that were not detected at least in 3 samples of the same group (either total cardiac tissue or exophers). Data in each sample was normalized by the total number of spectral countsand represented as scaled abundance for each protein, defined as follows:

$$\text{Protein "X" in sample En} = \frac{\text{Counts of protein "X" in sample En}}{\text{Average of counts for protein "X" in sample En and Hn}}$$

Where En is Exopher sample "n" and Hn is Heart sample from which the same exophers were obtained. We only considered proteins with adjusted p-values below 0.05 as significantly changed between both conditions, as shown in Fig.S2M.

RNA Isolation, reverse Transcription, and real-time PCR

Total RNA was prepared with RNA Extraction RNeasy Plus Micro-kit (QIAGEN) for isolation from macrophages or with TRIzol (Sigma) for total tissue RNA. RNA was reverse-transcribed with High-Capacity cDNA Reverse Transcription kit (Applied Biosystems; Carlsbad, CA) according to the manufacturer's protocol. Real-time quantitative PCR (SYBR-green, Applied Biosystems) assays were performed with an Applied Biosystems 7900HT Fast Real-Time PCR System sequencer detector. Expression was normalized to expression of the 36b4 housekeeping gene. Primer sequences were:

36b4: Fw(5´>3´)ACTGGTCTAGGACCCGAGAAG; Rv(5´>3´) TCCCACCTTGTCTCCAGTCT

Keima: Fw(5´>3´)AGCTTCAGTACGGAAGCATACC; Rv(5´>3´)TGCTCCTCTCCCATGTATATCC

Tomato: Fw(5´>3´)GCCGACATCCCCGATTACAAGA; Rv(5´>3´)CGATGGTGTAGTCCTCGTTGTGG

Mertk expression in cardiac cells

Cx3cr1 (to identify macrophages) and *Mertk* gene expressions were analyzed from a single cell sequencing dataset of cardiac cells publicly available in Tabula Muris (https://tabula-muris.ds.czbiohub.org/ and (Schaum et al., 2018)). Specifically, the FACS-based full length transcript dataset from the heart was used, as it has higher coverage and sensitivity than its droplet based counterpart. These results are presented in Fig.S7A as obtained by using the visualization

tool featured in Tabula Muris. In order to compare Mertk expression in cardiac macrophages with macrophages from other tissues, a heatmap plot was constructed using the normalized expression of relevant genes in heart, brain and spleen from the array data published by Pinto et al. (Pinto et al., 2012).

Quantification and Statistical Analysis

Data are represented as mean values ± standard error of the mean (SEM) or box and whiskers plots. Where applicable, normality was estimated using D'Agostino & Pearson or Shapiro-Wilk normality test. For comparison between 2 groups, paired or unpaired t-test was used when data presented normal distribution and paired or unpaired Mann-Withney when data did not follow normal distribution. For more than 2 groups, data were evaluated by one-way analysis of variance (ANOVA) with Dunnett's multiple comparison when data presented normal distribution and Kruskal-Wallis with Dunn´s multiple comparison when data did not follow normal distribution. Log-rank analysis was used for Mantel-Cox survival curves. Sample exclusion was not performed unless evident signs of disease were found in a mouse. Statistically significant outliers were identified using Grubb's test (ESD method). All statistical analyses were performed using Prism v6 (GraphPad Software, California, USA) and specified in the legends of every Figure. A p-value below 0.05 was considered statistically significant (*). P-values $p \leq 0.01$ (**) and $p \leq 0.001$ (***), as well as non-significant differences (n.s.) are indicated.

References

A-Gonzalez, N., Quintana, J.A., García-Silva, S., Mazariegos, M., de la Aleja, A.G., Nicolás-ávila, J.A., Walter, W., Adrover, J.M., Crainiciuc, G., Kuchroo, V.K., et al. (2017). Phagocytosis imprints heterogeneity in tissue-resident macrophages. J. Exp. Med. *214*, 1281–1296.

Acin-Perez, R., Lechuga-Vieco, A.V., DelMarMuñoz, M., Nieto-Arellano, R., Torroja, C., Sánchez-Cabo, F., Jiménez, C., González-Guerra, A., Carrascoso, I., Benincá, C., et al. (2018). Ablation of the stress protease OMA1 protects against heart failure in mice. Sci. Transl. Med. *10*.

Atkin-Smith, G.K., Paone, S., Zanker, D.J., Duan, M., Phan, T.K., Chen, W., Hulett, M.D., and Poon, I.K.H. (2017). Isolation of cell type-specific apoptotic bodies by fluorescence-activated cell sorting. Sci. Rep. *7*, 1–7.

Bensley, J.G., De Matteo, R., Harding, R., and Black, M.J. (2016). Three-dimensional direct measurement of cardiomyocyte volume, nuclearity, and ploidy in thick histological sections. Sci. Rep. *6*.

Bergmann, O., Bhardwaj, R.D., Bernard, S., Zdunek, S., Barnabé-Heide, F., Walsh, S., Zupicich, J., Alkass, K., Buchholz, B.A., Druid, H., et al. (2009). Evidence for cardiomyocyte renewal in humans. Science (80-.). *324*, 98–102.

Birch-Machin, M.A., and Turnbull, D.M. (2001). Assaying mitochondrial respiratory complex activity in mitochondria isolated from human cells and tissues. Methods Cell Biol. *65*, 97–117.

Bonzon-Kulichenko, E., Pérez-Hernández, D., Núñez, E., Martínez-Acedo, P., Navarro, P., Trevisan-Herraz, M., Del Carmen Ramos, M., Sierra, S., Martínez-Martínez, S., Ruiz-Meana, M., et al. (2011). A robust method for quantitative high-throughput analysis of proteomes by 18O labeling. Mol. Cell. Proteomics *10*.

Bonzon-Kulichenko, E., Garcia-Marques, F., Trevisan-Herraz, M., and Vázquez, J. (2015). Revisiting peptide identification by high-accuracy mass spectrometry: Problems associated with the use of narrow mass precursor windows. J. Proteome Res. *14*, 700–710.

Brooks, W.W., and Conrad, C.H. (2009). Isoproterenol-induced myocardial injury and diastolic dysfunction in mice: structural and functional correlates. Comp Med *59*, 339–343.

Burnett, S.H., Kershen, E.J., Zhang, J., Zeng, L., Straley, S.C., Kaplan, A.M., and Cohen, D.A. (2004). Conditional macrophage ablation in transgenic mice expressing a Fas-based suicide gene. J. Leukoc. Biol. *75*, 612–623.

Casanova-Acebes, M., Nicolás-Ávila, J.A., Li, J.L., García-Silva, S., Balachander, A., Rubio-Ponce, A., Weiss, L.A., Adrover, J.M., Burrows, K., A-González, N., et al. (2018). Neutrophils instruct homeostatic and pathological states in naive tissues. J. Exp. Med. jem.20181468.

Chakarov, S., Lim, H.Y., Tan, L., Lim, S.Y., See, P., Lum, J., Zhang, X.-M., Foo, S., Nakamizo, S., Duan, K., et al. (2019). Two distinct interstitial macrophage populations coexist across tissues in specific subtissular niches. Science (80-.). *363*, eaau0964.

Coll, R.C., Robertson, A.A.B., Chae, J.J., Higgins, S.C., Muñoz-Planillo, R., Inserra, M.C., Vetter, I., Dungan, L.S., Monks, B.G., Stutz, A., et al. (2015). A small-molecule inhibitor of the NLRP3 inflammasome for the treatment of inflammatory diseases. Nat. Med. *21*, 248–257.

Colombo, M., Raposo, G., and Théry, C. (2014). Biogenesis, Secretion, and Intercellular Interactions of Exosomes and Other Extracellular Vesicles. Annu. Rev. Cell Dev. Biol. *30*, 255–

289.

Cuezva, J.M., Chen, G., es MAlonso, A., Isidoro, A., EMisek, D., MHanash, S., and GBeer, D. (2004). The bioenergetic signature of lung adenocarcinomas is a molecular marker of cancer diagnosis and prognosis. Carcinogenesis.

Davies, L.C., Jenkins, S.J., Allen, J.E., and Taylor, P.R. (2013). Tissue-resident macrophages. Nat. Immunol. *14*, 986–995.

Davis, C.O., Kim, K.-Y., Bushong, E.A., Mills, E.A., Boassa, D., Shih, T., Kinebuchi, M., Phan, S., Zhou, Y., Bihlmeyer, N.A., et al. (2014). Transcellular degradation of axonal mitochondria. Proc. Natl. Acad. Sci. *111*, 9633–9638.

DeBerge, M., Yeap, X.Y., Dehn, S., Zhang, S., Grigoryeva, L., Misener, S., Procissi, D., Zhou, X., Lee, D.C., Muller, W.A., et al. (2017). MerTK cleavage on resident cardiac macrophages compromises repair after myocardial ischemia reperfusion injury. Circ. Res. *121*, 930–940.

Dick, S.A., Macklin, J.A., Nejat, S., Momen, A., Clemente-Casares, X., Althagafi, M.G., Chen, J., Kantores, C., Hosseinzadeh, S., Aronoff, L., et al. (2019). Self-renewing resident cardiac macrophages limit adverse remodeling following myocardial infarction. Nat. Immunol. *20*, 29–39.

Duvezin-Caubet, S., Jagasia, R., Wagener, J., Hofmann, S., Trifunovic, A., Hansson, A., Chomyn, A., Bauer, M.F., Attardi, G., Larsson, N.G., et al. (2006). Proteolytic processing of OPA1 links mitochondrial dysfunction to alterations in mitochondrial morphology. J. Biol. Chem. *281*, 37972–37979.

Epelman, S., Lavine, K.J., Beaudin, A.E., Sojka, D.K., Carrero, J.A., Calderon, B., Brija, T., Gautier, E.L., Ivanov, S., Satpathy, A.T., et al. (2014). Embryonic and adult-derived resident cardiac macrophages are maintained through distinct mechanisms at steady state and during inflammation. Immunity *40*, 91–104.

Faust, N., Varas, F., Kelly, L.M., Heck, S., and Graf, T. (2000). Insertion of enhanced green fluorescent protein into the lysozyme gene creates mice with green fluorescent granulocytes and macrophages. Blood *96*, 719–726.

García-Prat, L., Martínez-Vicente, M., Perdiguero, E., Ortet, L., Rodríguez-Ubreva, J., Rebollo, E., Ruiz-Bonilla, V., Gutarra, S., Ballestar, E., Serrano, A.L., et al. (2016). Autophagy maintains stemness by preventing senescence. Nature *529*, 37–42.

Gordon, S. (2016). Phagocytosis: An Immunobiologic Process. Immunity *44*, 463–475.

Hulsmans, M., Clauss, S., Xiao, L., Milan, D.J., Ellinor, P.T., Nahrendorf, M., Hulsmans, M., Clauss, S., Xiao, L., Aguirre, A.D., et al. (2017). Macrophages Facilitate Electrical Conduction in the Heart Article Macrophages Facilitate Electrical Conduction in the Heart. 510–522.

Joza, N., Susin, S.A., Daugas, E., Stanford, W.L., Cho, S.K., Li, C.Y.J., Sasaki, T., Elia, A.J., Cheng, H.Y.M., Ravagnan, L., et al. (2001). Essential role of the mitochondrial apoptosis-inducing factor in programmed cell death. Nature *410*, 549–554.

Jung, S., Aliberti, J., Graemmel, P., Sunshine, M.J., Kreutzberg, G.W., Sher, A., and Littman, D.R. (2000). Analysis of Fractalkine Receptor CX3CR1 Function by Targeted Deletion and Green Fluorescent Protein Reporter Gene Insertion. Mol. Cell. Biol. *20*, 4106–4114.

Katayama, H., Kogure, T., Mizushima, N., Yoshimori, T., and Miyawaki, A. (2011). A sensitive and quantitative technique for detecting autophagic events based on lysosomal delivery. Chem. Biol. *18*, 1042–1052.

Komatsu, M., Waguri, S., Ueno, T., Iwata, J., Murata, S., Tanida, I., Ezaki, J., Mizushima, N., Ohsumi, Y., Uchiyama, Y., et al. (2005). Impairment of starvation-induced and constitutive autophagy in Atg7-deficient mice. J. Cell Biol. *169*, 425–434.

Lapuente-Brun, E., Moreno-Loshuertos, R., Aciń-Pérez, R., Latorre-Pellicer, A., Colaś, C., Balsa, E., Perales-Clemente, E., Quirós, P.M., Calvo, E., Rodríguez-Hernández, M.A., et al. (2013). Supercomplex assembly determines electron flux in the mitochondrial electron transport chain. Science (80-.). *340*, 1567–1570.

Latorre-Pellicer, A., Moreno-Loshuertos, R., Lechuga-Vieco, A.V., Sánchez-Cabo, F., Torroja, C., Acín-Pérez, R., Calvo, E., Aix, E., González-Guerra, A., Logan, A., et al. (2016). Mitochondrial and nuclear DNA matching shapes metabolism and healthy ageing. Nature *535*, 561–565.

Lavine, K.J., Epelman, S., Uchida, K., Weber, K.J., Nichols, C.G., Schilling, J.D., Ornitz, D.M., Randolph, G.J., and Mann, D.L. (2014). Distinct macrophage lineages contribute to disparate patterns of cardiac recovery and remodeling in the neonatal and adult heart. Proc. Natl. Acad. Sci. U. S. A. *111*, 16029–16034.

Lemke, G. (2019). How macrophages deal with death. Nat. Rev. Immunol. *19*, 539–549.

Madisen, L., Zwingman, T.A., Sunkin, S.M., Oh, S.W., Zariwala, H.A., Gu, H., Ng, L.L., Palmiter, R.D., Hawrylycz, M.J., Jones, A.R., et al. (2010). A robust and high-throughput Cre reporting and characterization system for the whole mouse brain. Nat. Neurosci. *13*, 133–140.

Mai, S., Klinkenberg, M., Auburger, G., Bereiter-Hahn, J., and Jendrach, M. (2010). Decreased expression of Drp1 and Fis1 mediates mitochondrial elongation in senescent cells and enhances resistance to oxidative stress through PINK1. J. Cell Sci. *123*, 917–926.

Martínez-Bartolomé, S., Navarro, P., Martín-Maroto, F., López-Ferrer, D., Ramos-Fernández, A., Villar, M., García-Ruiz, J.P., and Vázquez, J. (2008). Properties of average score distributions of SEQUEST: The probability ratio method. Mol. Cell. Proteomics *7*, 1135–1145.

Melentijevic, I., Toth, M.L., Arnold, M.L., Guasp, R.J., Harinath, G., Nguyen, K.C., Taub, D., Parker, J.A., Neri, C., Gabel, C. V., et al. (2017). C. elegans neurons jettison protein aggregates and mitochondria under neurotoxic stress. Nature *542*, 367–371.

Miyake, Y., Asano, K., Kaise, H., Uemura, M., Nakayama, M., and Tanaka, M. (2007). Critical role of macrophages in the marginal zone in the suppression of immune responses to apoptotic cell-associated antigens. J. Clin. Invest. *117*, 2268–2278.

Mizushima, N., Yamamoto, A., Matsui, M., Yoshimori, T., and Ohsumi, Y. (2004). In Vivo Analysis of Autophagy in Response to Nutrient Starvation Using Transgenic Mice Expressing a Fluorescent Autophagosome Marker. Mol. Biol. Cell *15*, 1101–1111.

Molawi, K., Wolf, Y., Kandalla, P.K., Favret, J., Hagemeyer, N., Frenzel, K., Pinto, A.R., Klapproth, K., Henri, S., Malissen, B., et al. (2014). Progressive replacement of embryo-derived cardiac macrophages with age. J. Exp. Med. *211*.

Nahrendorf, M., and Swirski, F.K. (2013). Monocyte and macrophage heterogeneity in the heart. Circ. Res. *112*, 1624–1633.

Navarro, P., Trevisan-Herraz, M., Bonzon-Kulichenko, E., Núñez, E., Martínez-Acedo, P., Pérez-Hernández, D., Jorge, I., Mesa, R., Calvo, E., Carrascal, M., et al. (2014). General statistical framework for quantitative proteomics by stable isotope labeling. J. Proteome Res. *13*, 1234–1247.

Oka, T., Maillet, M., Watt, A.J., Schwartz, R.J., Aronow, B.J., Duncan, S.A., and Molkentin, J.D. (2006). Cardiac-specific deletion of gata4 reveals its requirement for hypertrophy, compensation, and myocyte viability. Circ. Res. *98*, 837–845.

Oka, T., Hikoso, S., Yamaguchi, O., Taneike, M., Takeda, T., Tamai, T., Oyabu, J., Murakawa, T., Nakayama, H., Nishida, K., et al. (2012). Mitochondrial DNA that escapes from autophagy causes inflammation and heart failure. Nature *485*, 251–255.

Pacher, P., Nagayama, T., Mukhopadhyay, P., Bátkai, S., and Kass, D.A. (2008). Measurement of cardiac function using pressure-volume conductance catheter technique in mice and rats. Nat. Protoc. *3*, 1422–1434.

Pinto, A.R., Paolicelli, R., Salimova, E., Gospocic, J., Slonimsky, E., Bilbao-Cortes, D., Godwin, J.W., and Rosenthal, N.A. (2012). An abundant tissue macrophage population in the adult murine heart with a distinct alternatively-activated macrophage profile. PLoS One *7*.

Quirós, P.M., Ramsay, A.J., Sala, D., Fernández-Vizarra, E., Rodríguez, F., Peinado, J.R., Fernández-García, M.S., Vega, J.A., Enríquez, J.A., Zorzano, A., et al. (2012). Loss of mitochondrial protease OMA1 alters processing of the GTPase OPA1 and causes obesity and defective thermogenesis in mice. EMBO J. *31*, 2117–2133.

Rawji, K.S., Mishra, M.K., Michaels, N.J., Rivest, S., Stys, P.K., and Wee Yong, V. (2016). Immunosenescence of microglia and macrophages: impact on the ageing central nervous system. Brain *139*, 653–661.

Schaum, N., Karkanias, J., Neff, N.F., May, A.P., Quake, S.R., Wyss-Coray, T., Darmanis, S., Batson, J., Botvinnik, O., Chen, M.B., et al. (2018). Single-cell transcriptomics of 20 mouse organs creates a Tabula Muris. Nature *562*, 367–372.

Sohal, D.S., Nghiem, M., Crackower, M.A., Witt, S.A., Kimball, T.R., Tymitz, K.M., Penninger, J.M., and Molkentin, J.D. (2001). Temporally regulated and tissue-specific gene manipulations in the adult and embryonic heart using a tamoxifen-inducible Cre protein. Circ. Res. *89*, 20–25.

Sörensen, I., Adams, R.H., and Gossler, A. (2009). DLL1-mediated Notch activation regulates endothelial identity in mouse fetal arteries. Blood *113*, 5680–5688.

Sousa, V.H., Miyoshi, G., Hjerling-Leffler, J., Karayannis, T., and Fishell, G. (2009). Characterization of Nkx6-2-Derived Neocortical Interneuron Lineages. Cereb. Cortex July *19*, 1–10.

Sun, N., Yun, J., Liu, J., Malide, D., Liu, C., Rovira, I.I., Holmström, K.M., Fergusson, M.M., Yoo, Y.H., Combs, C.A., et al. (2015). Measuring In Vivo Mitophagy. Mol. Cell *60*, 685–696.

Sun, N., Malide, D., Liu, J., Rovira, I.I., Combs, C.A., and Finkel, T. (2017). A fluorescence-based imaging method to measure in vitro and in vivo mitophagy using mt-Keima. Nat. Protoc. *12*, 1576–1587.

Tong, M., and Sadoshima, J. (2016). Mitochondrial autophagy in cardiomyopathy. Curr. Opin. Genet. Dev. *38*, 8–15.

Vintersten, K., Monetti, C., Gertsenstein, M., Zhang, P., Laszlo, L., Biechele, S., and Nagy, A. (2004). Mouse in red: Red fluorescent protein expression in mouse ES cells, embryos, and adult animals. Genesis *40*, 241–246.

Violot, S., Carpentier, P., Blanchoin, L., and Bourgeois, D. (2009). Reverse pH-dependence of chromophore protonation explains the large stokes shift of the red fluorescent protein mKeima. J.

Am. Chem. Soc. *131*, 10356–10357.

Vives-Bauza, C., Yang, L., and Manfredi, G. (2007). Assay of Mitochondrial ATP Synthesis in Animal Cells and Tissues. Methods Cell Biol. *80*, 155–171.

Wan, E., Yeap, X.Y., Dehn, S., Terry, R., Novak, M., Zhang, S., Iwata, S., Han, X., Homma, S., Drosatos, K., et al. (2013). Enhanced efferocytosis of apoptotic cardiomyocytes through myeloid-epithelial-reproductive tyrosine kinase links acute inflammation resolution to cardiac repair after infarction. Circ. Res. *113*, 1004–1012.

Xiao, X., Li, J., and Samulski, R.J. (1998). Production of high-titer recombinant adeno-associated virus vectors in the absence of helper adenovirus. J. Virol. *72*, 2224–2232.

Yu, J., Nagasu, H., Murakami, T., Hoang, H., Broderick, L., Hoffman, H.M., and Horng, T. (2014). Inflammasome activation leads to Caspase-1-dependent mitochondrial damage and block of mitophagy. Proc. Natl. Acad. Sci. U. S. A. *111*, 15514–15519.

Zhou, R., Yazdi, A.S., Menu, P., and Tschopp, J. (2011). A role for mitochondria in NLRP3 inflammasome activation. Nature *469*, 221–226.
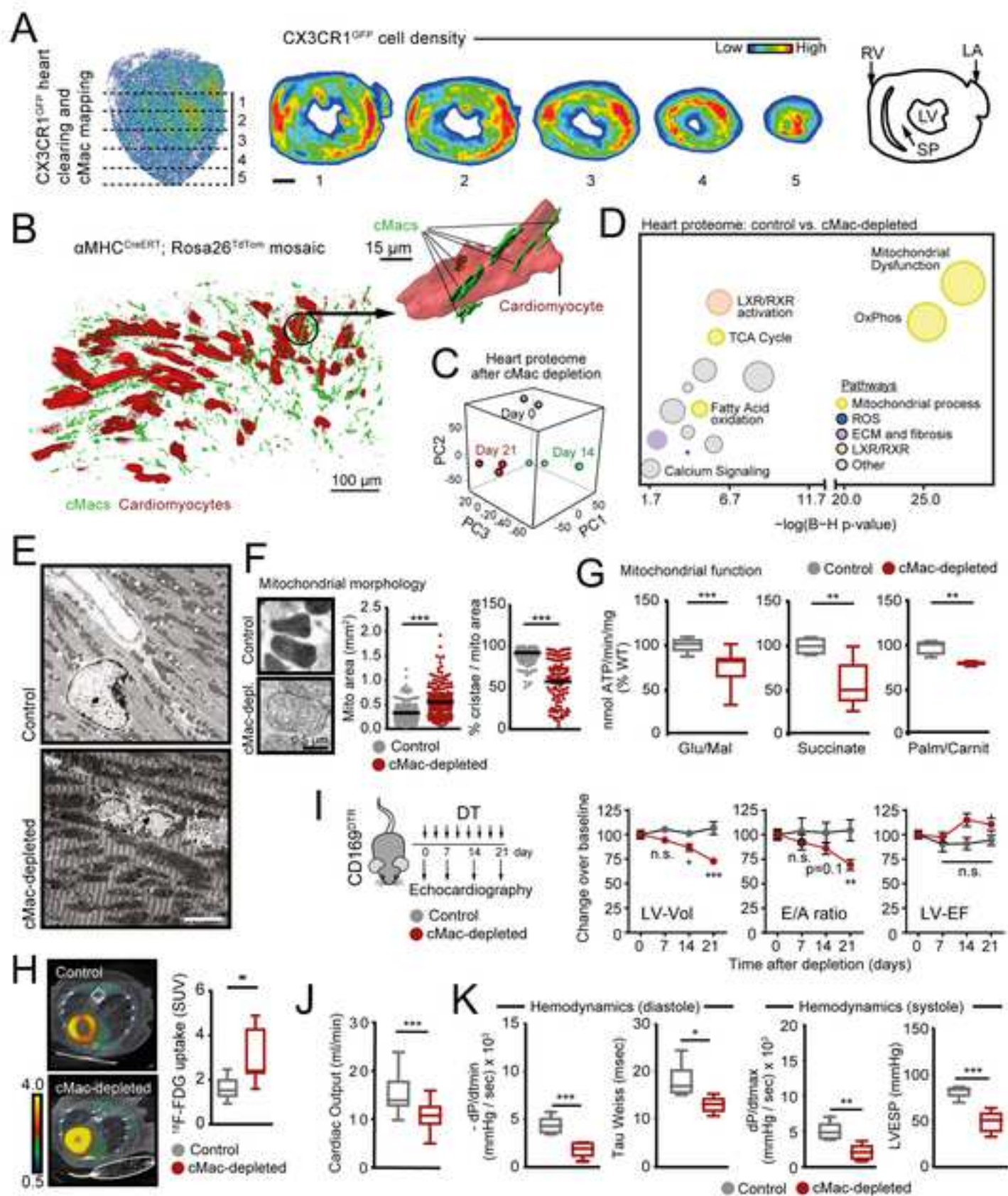
KEY RESOURCES TABLE

REAGENT or RESOURCE	SOURCE	IDENTIFIER
Antibodies		
Anti-CD45-PerCP.Cy5.5 (clone 30-F11)	Biolegend	CAT# 103132
Anti-CD45.1-PerCP.Cy5.5 (clone A20)	TonboBioscience	CAT# 65-0453
Anti-CD45.2-FITC (clone 104)	eBioscience	CAT# 11-0454-82
Anti-CD45.2-APC.Cy7 (clone 104)	eBioscience	CAT# 47-0454-82
Anti-CD11b-PE (clone M1/70)	TonboBioscience	CAT# 50-0112
Anti-CD11b-Bv510 (clone M1/70)	Biolegend	CAT# 101245
Anti-CD11b-APC (clone M1/70)	TonboBioscience	CAT# 20-0112
Anti-F4/80-biotin (clone BM8)	eBioscience	CAT# 13-4801-82
Anti-F4/80-APC (clone BM8)	eBioscience	CAT# 17-4801-82
Anti-F4/80-PE.Cy7 (clone BM8)	eBioscience	CAT# 25-4801-82
Anti-MHCII-PE.Cy7 (clone M5/114.15.2)	Biolegend	CAT# 107630
Anti-MHCII-Biotin (clone M5/114.15.2)	Biolegend	CAT# 107604
Anti-Ly6C-FITC (clone HK1.4)	Biolegend	CAT# 128006
Anti-CD31-Bv605 (clone 390)	Biolegend	CAT# 102427
Streptavidin-eF780	eBioscience	CAT# 12-4317-87
Streptavidin-PE	eBioscience	CAT# 12-4317-87
Streptavidin-DyLight649	JacksonImmunoresearch	CAT# SA-5649
Rat Anti-CD68 (clone FA-11)	BioRad	CAT# MCA1957
Rat Anti-CD169 (clone 3D6)	kindly provided by S.Gordon	n/a
Rabbit Anti-laminin (polyclonal)	Sigma	CAT# L9393
Rabbit Anti-NDUFS2 (polyclonal)	Abcam	CAT# ab216510
Rabbit Anti-CytochromeC (clone EPR1327)	Abcam	CAT# ab133504
Rabbit Anti-Tom20 (clone FL-145)	SantaCruzBiotechnology	CAT# sc-11415
Rabbit Anti-Myh7 (clone NOQ7.5.4D)	Sigma	CAT# HPA001239
Rabbit Anti-LAMP1 (polyclonal)	Sigma	CAT# L1418
Mouse Anti-LC3 (clone 5F10)	Nanotools	CAT# 0231-100/LC3-5F10
Armenian Hamster Anti-CD31 (clone 2H8)	Merck	CAT# MAB1398Z
Rabbit Anti-RFP (polyclonal)	Rockland	CAT# 600-401-379
Chicken Anti-GFP (polyclonal)	Abcam	CAT# ab13970
Mouse Anti-CD68 (clone PG-M1)	Dako	CAT# ab783
Mouse Anti-MYH (clone MF20)	DSHB hybridoma	CAT# Product MF20
Goat Anti-rat (polyclonal)	MolecularProbes	CAT# A22287
Mouse Anti-NLRP3 (clone 25N10E9)	ThermoFisher	CAT# MA5-16274
Mouse Anti-Caspase-1 (clone 14F468)	SantaCruz	CAT# sc-56036
Rabbit Anti-LC3 (polyclonal)	CellSignal	CAT# 2775S
Rabbit Anti-p62 (polyclonal)	CellSignal	CAT# 5114S
Rabbit Anti-Optineurin (clone EPR20654)	Abcam	CAT# ab213556
Rabbit Anti-PEX14 (Ployclonal)	Proteintech	CAT# 10594-1-AP
Rabbit Anti-GM130 (clone EP892Y)	Abcam	CAT# ab52649

Mouse Anti-Keima (clone 1C3)	MBL Life Science	CAT# M182-3M
Chicken Anti-GFP (polyclonal)	Invitrogen	CAT# A10262
Bacterial and Virus Strains		
AAV-mtKeima	This Manuscript	n/a
Biological Samples		
Human papillary muscle biopsies	Hospital Universitario de la Princesa (Madrid)	n/a
Chemicals, Peptides, and Recombinant Proteins		
Isoproterenol	Sigma Aldrich	CAT# 1351005
Diphteria Toxin	Calbiochem	CAT# 322326
Rapamycin	LC Laboratories	CAT# NC9163747
MCC950	Merck	CAT# PZ0280
Critical Commercial Assays		
MitoNIR	Abcam	CAT# ab176833
Mitotracker Deep Red	ThermoFisher	CAT# M22426
In Situ Cell Death Detection Kit	Roche	CAT# 11684795910
Deposited Data		
CD169^{DTR} vs Control Heart Proteomics	This Manuscript	Peptide Atlas: PASS01430
Exopher proteomics	This Manuscript	Peptide Atlas: PASS01151
Experimental Models: Organisms/Strains		
Mice: C57BL/6JOlaHsd	Envigo	CAT# 057
Mice: C57BL/6J	Jackson Labs	CAT# 000664
Mice: B6.129P2(Cg)-Cx3cr1^{tm1Litt}/J	Steffen Jung	Jung et al., 2000
Mice: Lyz2$^{tm1.1Graf}$	Thomas Graf	Faust et al., 2000
Mice: C57BL/6-Tg(Csf1r-EGFP-NGFR/FKBP1A/TNFRSF6)2Bck/J	Jackson Labs	Burnett et al., 2004
Mice: Tg(CAG-EGFP/Map1lc3b)53Nmz	Guillermo Mariño	Mizushima et al., 2004
Mice: B6.FVB-Tg(Myh6-cre)2182Mds/J	Jose Luis de la Pompa	Oka et al., 2000
Mice: B6.FVB(129)-A1cf$^{Tg(Myh6-cre/Esr1*)1Jmk}$/J	Juan Miguel Redondo	Sohal et al., 2001
Mice: C57BL/6-Tg(Cdh5-cre/ERT2)1Rha	Ralf Adams	Sorensen et al., 2009
Mice: Gt(ROSA)26Sor$^{tm9(CAG-tdTomato)Hze}$	Miguel Torres	Madisen et al., 2010
Mice: Gt(ROSA)26Sor$^{tm1.1(CAG-EGFP)Fsh/Mmjax}$	Miguel Torres	Sousa et al., 2009
Mice: Atg7^{tm1Tchi}	Marco Sandri	Komatsu et al., 2005
Mice: Tg(CAG-DsRed*MST)1Nagy/J	Ignacio Flores	Vintersten et al., 2004
Mice: Siglec1$^{tm1(HBEGF)Mtka}$	Masato Tanaka	Miyake et al., 2007
Mice: OMA1$^{-/-}$	Carlos Lopez-Otín	n/a
Mice: B6.SJL-$Ptprc^a$ $Pepc^b$/BoyJ	Jackson Laboratories	JAX: 002014
Mice: BL/6^{NzB}	Jose Antonio Enriquez	Latorre-Pellicer et al., 2016
Mice: Mertk$^{-/-}$	Antonio Castrillo	Lu et al.1999
Cell lines		
HL1^{GFP}	Juan Bernal	This Work
Oligonucleotides		
Fw (5´-3´) Primer for 36B4 gene: ACTGGTCTAGGACCCGAGAAG	This Manuscript	N/A
Rv (5´-3´) Primer for 36B4 gene: TCCCACCTTGTCTCCAGTCT	This Manuscript	N/A
Fw (5´-3´) Primer for Keima gene: AGCTTCAGTACGGAAGCATACC	This Manuscript	N/A

Rv (5´-3´) Primer for Keima gene: TGCTCCTCTCCCATGTATATCC	This Manuscript	N/A
Fw (5´-3´) Primer for Tomato gene: GCCGACATCCCCGATTACAAGA	This Manuscript	N/A
Rv (5´-3´) Primer for Tomato gene: CGATGGTGTAGTCCTCGTTGTGG	This Manuscript	N/A
Fw (5´-3´) Primer to distinguish NzB and C57 mtDNA: AAGCTATCGGGCCCATACCCCG	This Manuscript	N/A
Rv (5´-3´) Primer to distinguish NzB and C57 mtDNA: GTTGAGTAGAGTGAGGGATGGG	This Manuscript	N/A
Recombinant DNA		
Plasmid mt-Keima-Red-Mito-7	Michael Davidson	Addgene plasmid # 56018
Software and Algorithms		
ImageJ	Schneider et al., 2012	https://imagej.nih.gov/ij/
Imaris	Bitplane	https://imaris.oxinst.com/packages
Prism	Graphpad	https://www.graphpad.com/scientific-software/prism/

Figure 1

Figure 2

Figure 3

A

B Card^RED Tom20
Card^RED
Tom20

C CD68
DAPI
Exophers
Tom20

D Heart Intestine BM
NZB
C57
NZB
C57
Spleen Liver Skeletal Muscle

% C57 mtDNA
** *** *** ** n.s.
Heart Intestine BM Spleen Liver Skeletal Muscle

E DAPI mt-Keima CD68 Merge
cMac

F Cardiomyocyte Keima CD68 DAPI

G Keima
C57 mtDNA
% signal in Macs
Hours in culture
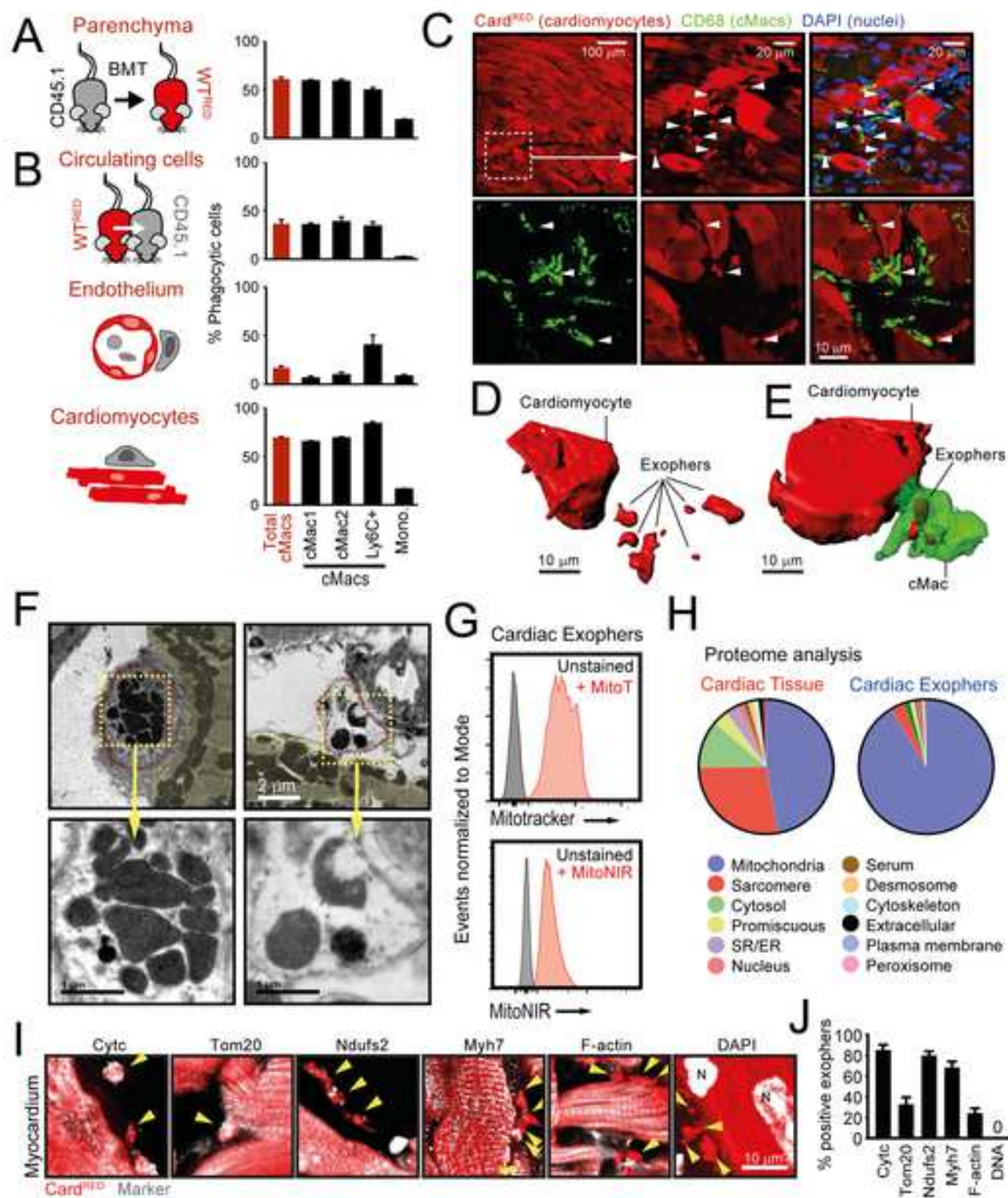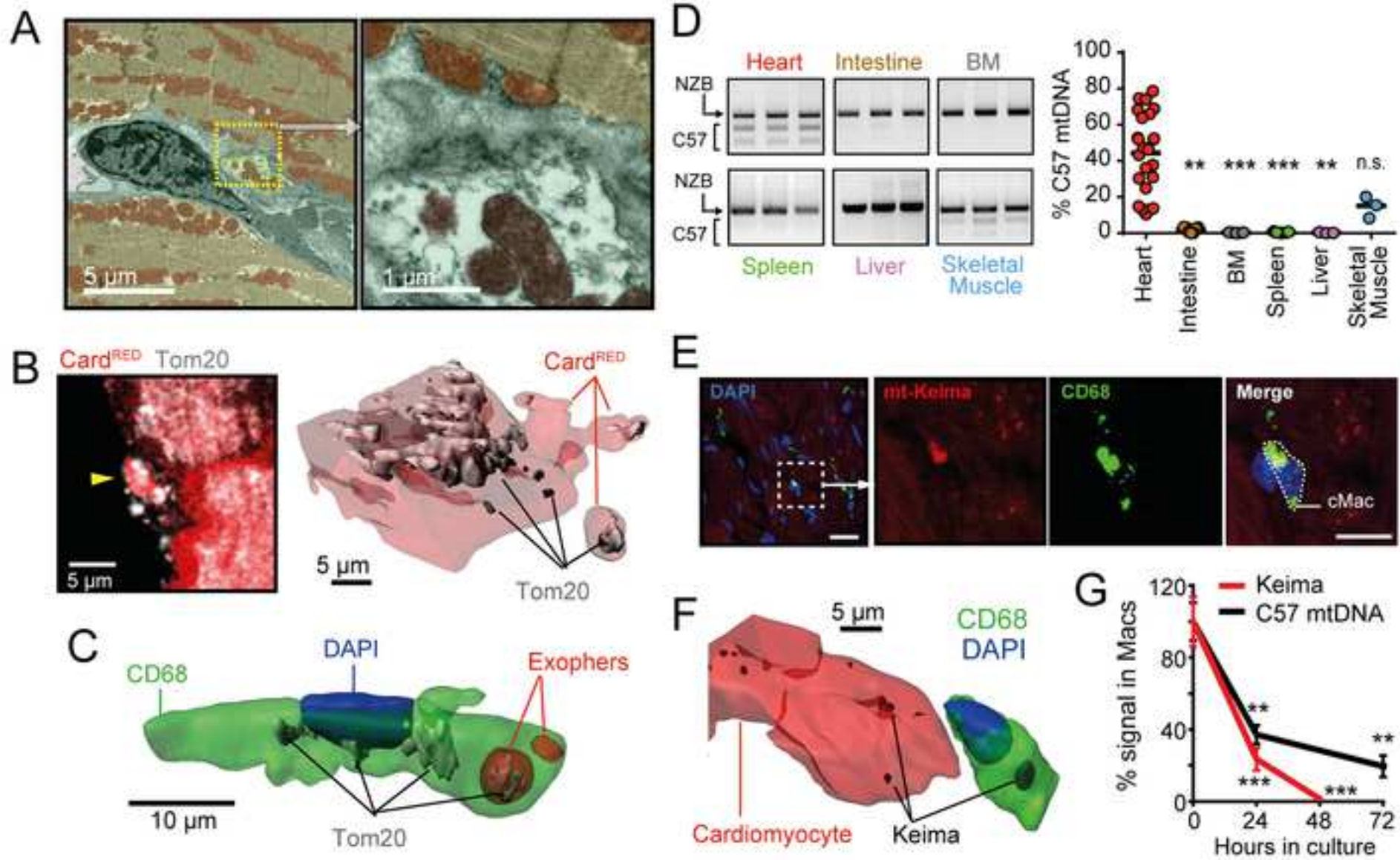
Figure 4

Figure 5

Figure 6

Figure 7

Supplemental Information for

A network of macrophages supports mitochondrial homeostasis in the heart

Nicolas-Avila, Lechuga-Vieco, et al.

This document contains the supplementary figure legends, tables and supplementary video legends for "A network of macrophages supports mitochondrial homeostasis in the heart". CELL-D-19-02934R2
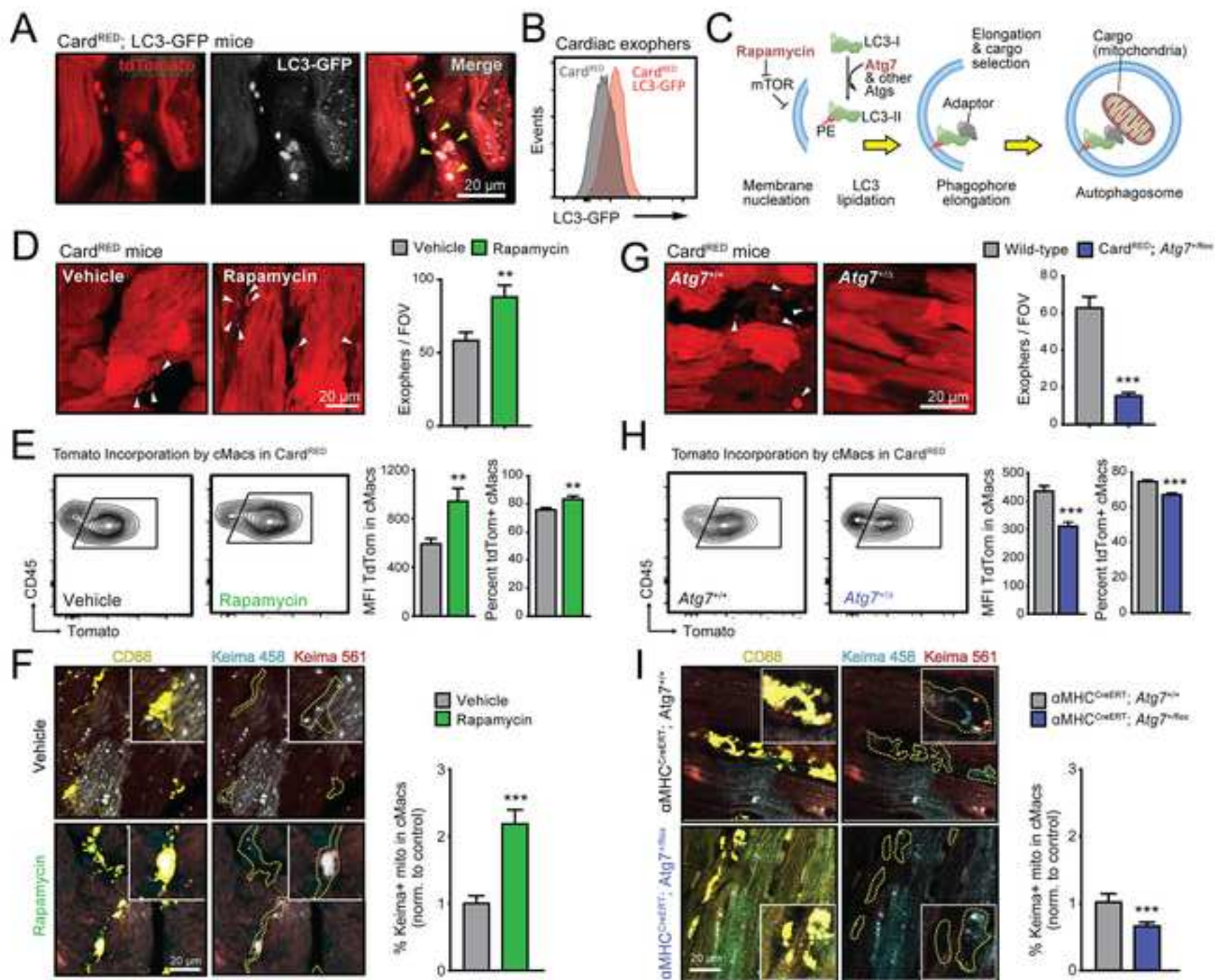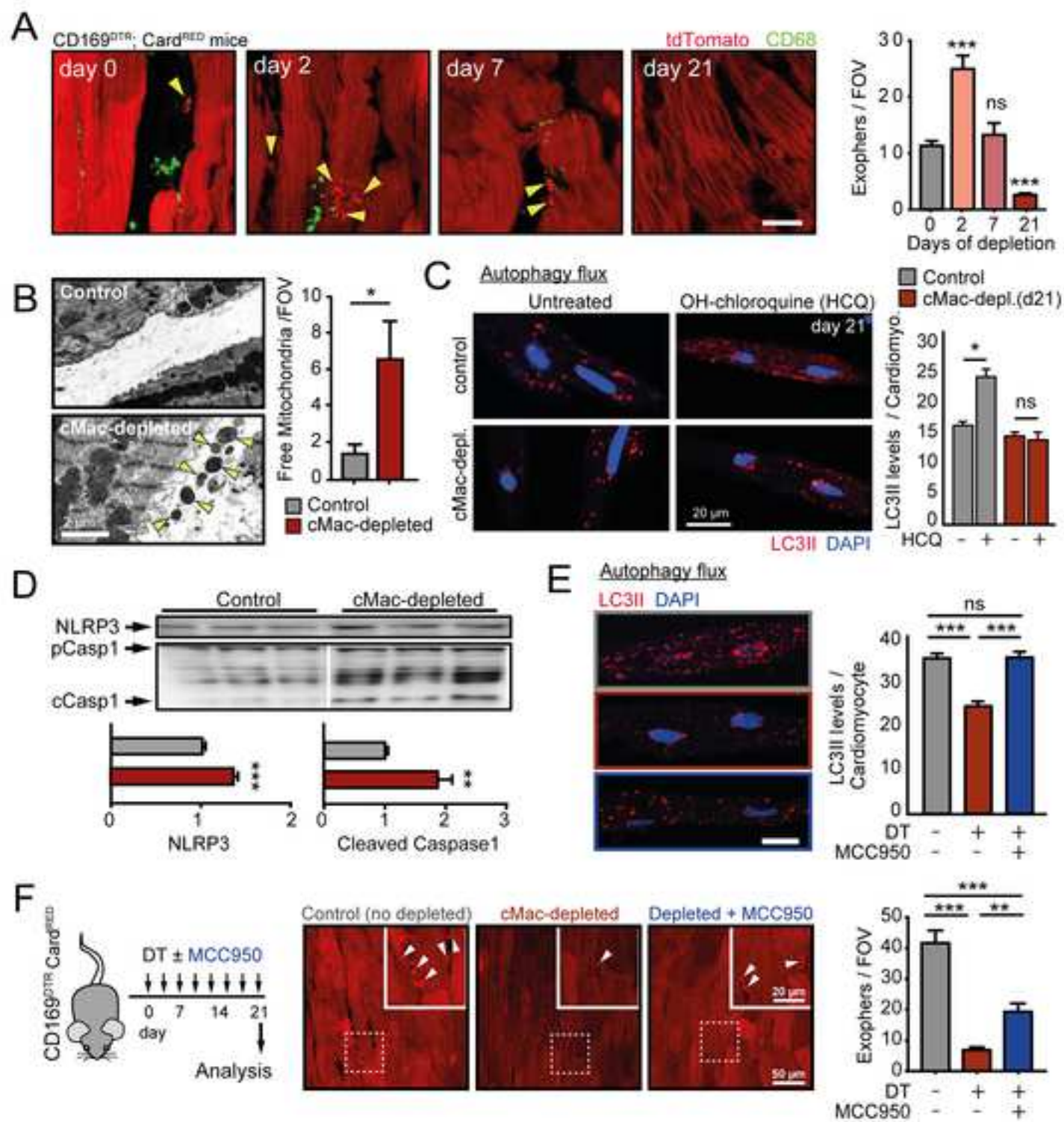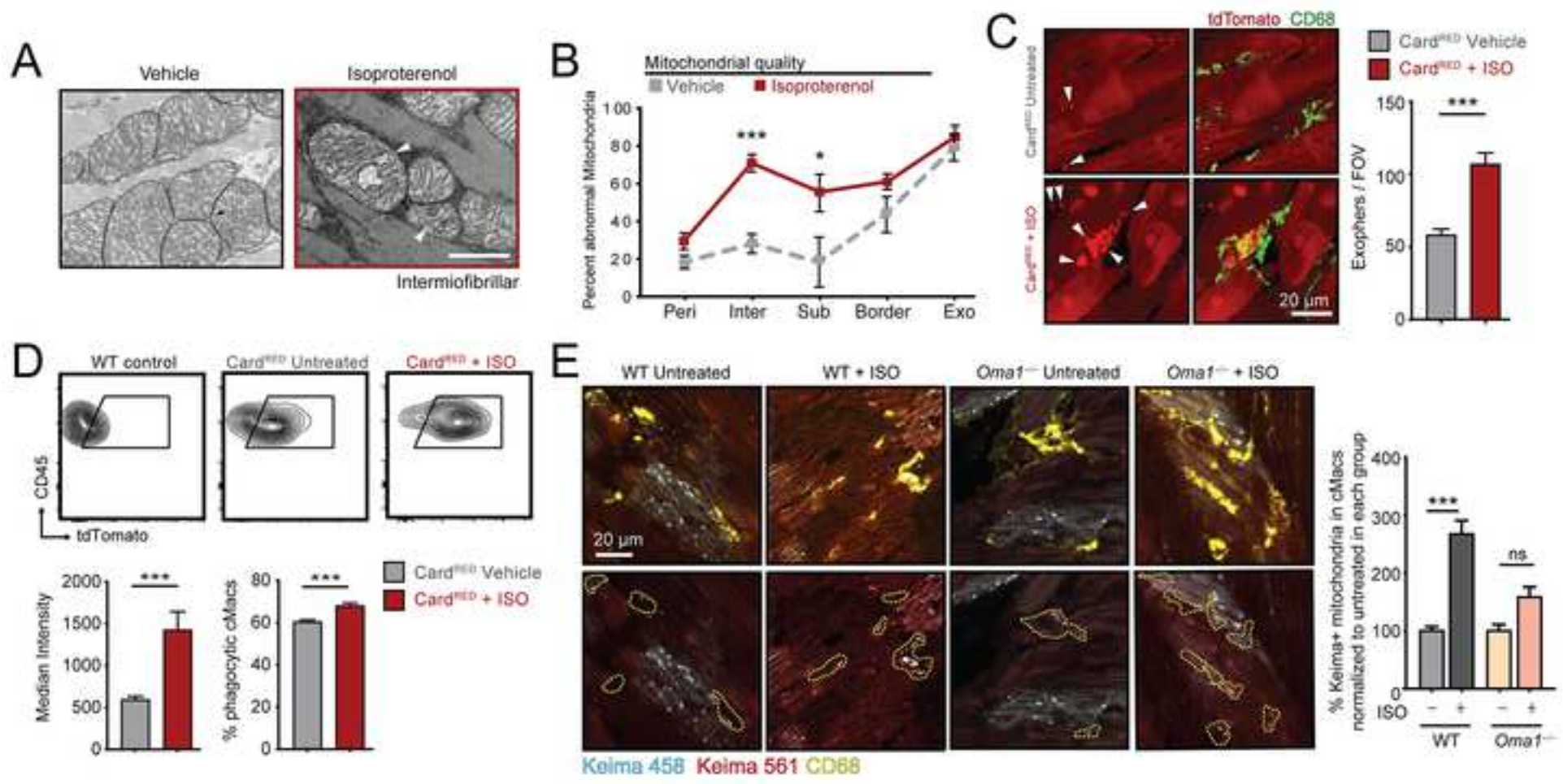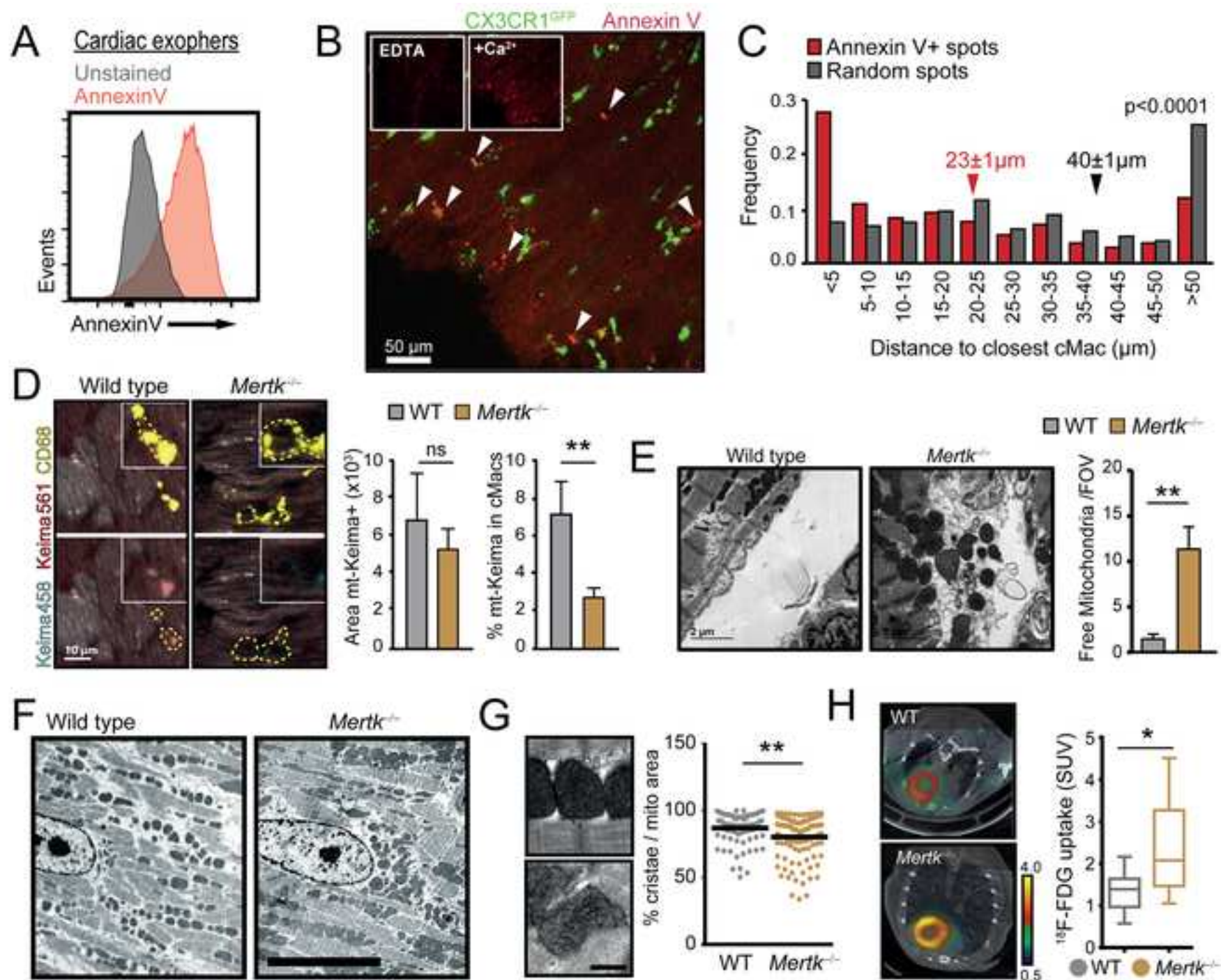
Figure S1. Features of cMac in the ventricular myocardium, related to **Figure 1.**
(A) Gating strategy used to identify cardiac macrophage subsets by flow cytometry.
(B) Percentage of GFP+ out of total cMacs in CX3CR1^{GFP}, LysM^{GFP} and Csf1r^{GFP} reporter mice. Data are mean ± SEM from 3-6 mice per group.
(C) Heart imaging. 3D reconstruction of a whole cleared heart from CX3CR1^{GFP} mice, showing the distribution of vessels (CD31, white) and cMacs (CX3CR1^{GFP}+ cells, green). Image at right is a high-magnification raw image of the myocardium showing the distribution of cMacs over the autofluorescent tissue. Scale bars, 1 mm (left panel) and 100 μm (right). See Video S1.
(D-E) Micrographs of hearts from CX3CR1^{GFP} mice and matched schemes (left panels) illustrating contacts between cardiomyocytes, which are defined by the staining of their basal lamina with anti-laminin (red) and cMacs (green) in transversal **(D)** or longitudinal sections **(E)**. Scale bars, 20 μm (D) and 50 μm (E). Right, quantification of the number of interactions as determined form images as in panels (D-E). Bar graphs show mean ± SEM from 3 mice; CM, cardiomyocyte.
(F) Immunofluorescence staining of CD169 (red) in myocardial tissue showing protein only in CX3CR1^{GFP}+ cMacs (green). Nuclei (DAPI) are blue. Scale bar, 10 μm.
(G) Long-term depletion of the various subsets of cMacs in CD169^{DTR} mice treated with DT thrice per week, and analysed on days 0, 2, 7, 14 and 21. Data are mean number of cMacs (relative to t=0) ± SEM from 3 mice per group. ***, p<0.001, as determined by one-way ANOVA with Dunnett's multiple comparisons test against t= 0.
(H) Heat map showing cardiac proteins differentially detected between days 0 and 21, with values for day 14 also shown. Z-scores values are given in the colour scale. Proteins are grouped in categories according to their presence in mitochondria or other structures (e.g., sarcomere or ECM), or the functional pathway in which they are involved.
(I-J) Increased mitochondria in cMac-depleted hearts. **(I)** Representative TEM images and **(J)** mitochondrial content in cardiomyocytes determined from TEM images (top) and by Tom20 immunofluorescence (bottom) analyses, in control and cMac-depleted mice (day 21). Scale bar, 10 μm. Box and Wishker plots show mean ± SEM from n= 9-10 mice per group; *, p<0.05 as determined by unpaired t-test.
(K) Citrate synthase activity in undepleted control and cMac-depleted mice (CD169^{DTR}+DT). Box and whisker graphs shows enzymatic activity per mg of total protein from heart or liver, normalized to the control group; n= 6-12 mice per group. *, p<0.05; n.s., not significant, as determined by unpaired t-test against control groups.
(L) Macrophage numbers in hearts and livers of CD169^{DTR} mice treated with saline (control) or DT for 7 days. ***, p<0.001, as determined by unpaired t-test.
(M) Ex vivo ATP production rates in purified mitochondria from control and cMac-depleted livers in the presence of the indicated substrates. Values are shown as box and whiskers, and normalized to the control groups. Data from 6-7 mice per group. n.s, not significant, as determined by unpaired t-test. Glu/Mal, glutamate plus malate.
(N) Changes in ATPb/GADPH ratios (BEC index) assessed by western blot (left) in heart extracts of control and cMac-depleted hearts. α-actin protein was used for load control. Data are presented as box and whiskers, from 4 mice per group. *, p<0.05 as determined by unpaired t-test.
(O) High-energy phosphate metabolites in hearts from control (WT+DT) and cMac-depleted (CD169^{DTR} + DT) mice. The graph shows pCreatine (PCr)/ATP ratios measured in vivo by quantitative magnetic resonance spectroscopy (^{31}P-MRS). Values are presented as box and whiskers, from 4-6 mice per group. **, p<0.01 as determined by unpaired t-test.
(P) Left, experimental scheme to analyze cardiac function by echocardiography after cMac recovery from depletion (right).
(Q) Selected echocardiographic parameters were measured in CD169^{DTR} mice treated with DT for 21 days, and then allowed to recover in the absence of DT as in panel (P).

Echocardiography measures were obtained longitudinally at the indicated times in the same mice. Data are mean ± SEM normalized to day 0, from 12 mice per group. *, $p<0.05$; **, $p<0.01$; ***, $p<0.001$; n.s., not significant, as determined by Student's t-test analysis against day 0. LV, left ventricle; Vol, volume.

Controls for all cMac-depletion experiments were wild-type mice treated with DT.

Figure S2. cMacs phagocytose cardiomyocyte-derived material, related to **Figure 2.**

(A) Bright-field images of sorted and cytospined cardiac leukocytes corresponding to the subsets in (Fig.S1A), and stained with Giemsa. Note the presence of large phagolysosomes-like vacuoles in cMacs that are absent in monocytes.

(B-C) Cytometric identification of phagocytic cells in the heart of the indicated mouse models (see also Figure 2A-B). Plots show the percentage of F4/80+CD11b+ cells (Macs) within CD45.1+ or CD45+ leukocytes that engulf DsRed+/Tomato+ material (left plots) from parenchymal cells (CD45.1 BM transplanted into WT^{RED} mice) **(B)**, or in circulating cells (WT^{RED} x CD45.1 parabionts), endothelial cells (Cadh5^{CreERT} Rosa26^{TdTom}), or cardiomyocytes (αMHC^{Cre} Rosa26^{TdTom}; Card^{RED}) **(C)**. Also, density plots show the uptake of TdTomato red fluorescence by total CD45+ leukocytes (middle plots) or by cMacs (right plots) in control and experimental mice. Values in plots are mean ± SEM, n=3-6 mice, as shown for cMacs in Fig.2A-B.

(D) Volumes of cardiac exophers and cMacs reconstructed by confocal imaging from hearts of Card^{RED} mice stained with anti-CD68 (see also Figure 2D-E and Video S3). Dot plots show mean volumes, from 8 mice per group. ***, p<0.001 as determined by nonparametric Mann-Whitney test.

(E) Percentage of cardiac exophers that are associated or not-associated ("Free") with cMacs. The bar graph shows mean ± SEM percentages; n= 40 images from 4 mice.

(F) (Left) Immunofluorescence of myocardium from Card^{RED} mice showing the distribution of Cardiac exophers (red, highlighted by yellow arrows) or Random spots (grey), used to measure the distances to the closest cMac. Bars at right show mean ± SEM distances for each group. Data from 30 images from 3 mice. P-value was obtained by nonparametric Mann-Whitney test.

(G) Expression of tdTomato transcript in total cardiac tissue, which is undetectealbe in cMacs from Card^{RED} mice, as determined by qPCR. Bars shows mean ± SEM from 10-11 mice per group of 2 independent experiments. ***, p<0.01, as determined by Student's ttest.

(H) Representative TEM images of mitochondria- and sarcomere-containing structures surrounded by membranes in murine hearts. Scale bars (left to right) are 5, 2 and 1 µm. Images are representative of 5 hearts. Mitochondria and sarcomere are indicated with green and orange arrows, respectively.

(I) TEM imaging of similar structures in human hearts. Scale bars (left to right) are 2 and 0.5 µm. Exophers are outlined by a red dashed line, and adjacent cardiomyocytes by a yellow mask (labelled "C"). Images are representative of 5 hearts.

(J) Immunofluorescence micrographs of human myocardia obtained from surgical resections of papillary muscles stained for macrophages (CD68, green), nuclei (DAPI, blue) and sarcomere /cardiomyocytes (MyHC; red). Images are representative of 5 samples. Scale bar, 20 µm.

(K) Strategy for enrichment and purification of cardiac exophers by serial sedimentation and centrifugation, as detailed in Methods. The gating strategy used to define exophers by FACS in the 1000g pellet of Card^{RED} mice is shown in the cytometry plots.

(L) Immunofluorescence of pellets from the 50, 300 and 1000g fractions and isolated cardiac exophers from Card^{RED} mice (as defined in (A)). Nuclei (DAPI, blue), autofluorescence (green) and tdTomato (Red). Scale bar 15 µm. Images are representative of 3 mice per group.

(M) List of proteins and their relative abundance in total cardiac (red dots) and exopher (blue dots) proteomes annotated for each cellular compartment. Values are given as mean scaled abundances (see Methods).

(N) (Left) Representative images of left ventricular sections from Card^{RED} mice (tdTomato protein, red) stained for the indicated proteins (white) to assess their presence in exophers

4

(yellow arrowheads). (Right) Fraction of exophers positive for the proteins shown. Bars are mean ± SEM from 3-5 mice. See also Figure 2I-J. Scale bar, 10 μm.

Figure S3. cMacs take up cardiomyocyte-derived mitochondria, related to **Figure 3.**

(A) Experimental strategy to track cardiomyocyte-derived mitochondrial DNA (mtDNA) in cMacs after bone marrow transplantation. cMacs from BL/6^{NZB} donors that take up mitochondria in BL/6.SJL^{C57} hearts (pink) are sort-purified and analyzed by PCR to determine the amount of parenchymal C57-mtDNA after BamHI digestion. This allows discrimination of polymorphisms among the two mtDNA haplotypes. Note that while BL/6^{NZB}-derived cMacs contain both NZB and C57-mtDNA, BL/6.SJL^{C57}-derived cMacs only carry C57-mtDNA, indicating specificity and no cross-contamination during cMac sorting. Percentages of donor- and host-derived cardiac macrophages are shown. Numbers are mean ± SEM, from 8 mice.

(B) Experimental design to tag cardiomyocyte mitochondria with mt-Keima. Mice were injected with AAV9 encoding mitochondrial-targeted Keima fluorescent protein (mt-Keima) and expression driven by a cardiomyocyte-specific promoter (*Tnnt2*). Images at bottom illustrate the progressive acquisition of mt-Keima fluorescence in infected hearts at weeks 0, 2 and 5 post infection. Scale bars, 20 µm.

(C) Expression of mt-Keima transcript in total cardiac tissue but not in cMacs 6 weeks after infection, as determined by qPCR. Bars shows mean ± SEM from 4 mice per group. ND: Not detected.

(D-E) αMHC^{Cre}; Rosa26^{TdEGFP} mice, referred to as Card^{GREEN}, were infected with AAV9-mt-keima and sacrificed after 5 weeks. **(D)** Micrographs with signals for keima 561nm peak (red), cardiomyocytes (GFP, green) and exophers (GFP, green; indicated by white arrows) are shown. **(E)** Images of sorted exophers from these mice showing signals for Keima (Red) and GFP (green). Scale bars 20 µm

(F-H) Distribution of mt-Keima in infected hearts. **(F)** Micrographs illustrating pH-dependent mt-Keima fluorescence. Images show Keima-tagged mitochondria in non-acidic (Keima 458nm; Cyan) and acidic (Keima 561nm; red) environments. Dark blue, DAPI. Scale bars, 10 µm (large images) and 5 µm (insets). The images are quantifed in the bar graph, showing that the majority of mitochondria inside cMacs are "acidic" (high 561/456nm ratios) while most mitochondria inside cardiomyocytes (CM) are "non-acidic" (low 561/456nm ratios). **(G)** Percentage of mt-Keima signal localized inside LAMP1+ or LAMP^{NEG} compartments in cMacs. Bars show mean ± SEM from 45 images, from 3 mice. See also Video S4.

(H) Percentage of "acidic" Keima+ mitochondria (561nm signal>458nm signal) inside CM or in cMacs. Data are mean ± SEM from 15 images and 3 mice per group. *, $p<0.05$, determined by a nonparametric Mann-Whitney test.

(I) Micrograph of live cardiomyocyte-macrophage co-cultures. Images at right show three insets with dynamic material exchange between HL1^{GFP} cardiomyocytes (green) and DsRed+ macrophages (red). Images representative of 3 experiments. See also Video S5. Scale bar, 20 µm.

(J) Micrograph of fixated macrophage-HL1^{GFP} co-cultures, showing HL1^{GFP} cardiomyocytes (green), mitochondria (grey; Tom20) and nuclei (Blue; DAPI). Indicated are exophers containing or not mitochondria (yellow and pink arrowheads, respectively). Scale bar is 20 µm.

(K) Comparison between HL1^{GFP}–derived exophers like particles and cardiac exophers from Card^{RED} tissue (as in Figure 2I-J). Dot plot at left shows diameter and the bar graph at right shows the percentage of particles staining positive for Tom20. Data is from 256 exophers from 3-4 animals.

Figure S4. Exophers transport dysfunctional mitochondria, related to **Figure 4.**

(A) Heatmap of proteins associated with mitochondrial fitness that significantly decreased in exophers when compared with total cardiac tissue (see also Fig.S2M). Adjusted p-value <0.05. Values are given as scaled abundances (see Methods).

(B) Representative TEM images of bubble-like structures containing mitochondria at the border zone (red arrowheads) of cardiomyocytes. Scale bar, 1 µm.

(C) TEM micrographs illustrating Normal (preserved integrity) and an Abnormal (damaged outer membranes, cristae or both) mitochondria and used for classification in (D-E). Scale bar, 1 µm.

(D) Scheme and representative images of mitochondria in different regions of cardiomyocytes (arrowheads). Scale bars, 2 µm.

(E) Percentage of mitochondria classified as Normal, Abnormal (see panel (C)) or Unclassified (not obvious alterations at this resolution). Regions were defined as in panel (D); data are from a total of 1208-1289 mitochondria scored from 3 mice per group.

(F) Mitochondrial membrane potential in cultured fibroblasts, cardiac leukocytes or cardiac exophers as assessed by mitoNIR uptake in basal conditions, and in the presence of depolarizing (FCCP) or hyperpolarizing (Oligomycin) agents. Bars show mean ± SEM from 4-5 samples per group and 2 independent experiments. *, $p<0.05$; **, $p<0.01$; ***, $p<0.001$; n.s., not significant as determined by multiple t-test vs MitoNIR incubated sample without treatment in each group.

(G) Citrate synthase (CS) activity in cardiomyocytes and cardiac exophers isolated form the same hearts. Bars are mean ± SEM from 6 mice per group from two independent experiments. *, $p<0.05$; as determined by paired t-test.

(H) Autophagy flux of *Atg7*-hemizygous mice. Left, immunofluorescence images of LC3 (red) and nuclei (DAPI, blue) in αMHC^{CRE}; Atg7$^{flox/+}$ and WT animals at baseline and 12 hours after incubation with hydroxychloroquine (HCQ). Bars show mean ± SEM of LC3 puncta per cardiomyocyte from 300 cells and 3 mice per group. Scale bar, 20 µm. ***, $p<0.001$; n.s., not significant as determined by Kruskal-Wallis with Dunn's multiple comparisons test against untreated.

(I) Survival curves of αMHC^{CreERT} crossed with Atg7$^{+/+}$, Atg7$^{flox/+}$, Atg7$^{flox/flox}$ after recombination induced by tamoxifen. *, $p<0.05$; ***, $p<0.001$ as determined by Log-rank for Mantel-Cox survival curves; data from 8-14 mice per group.

Figure S5. Inflammasome and autophagy alterations in cMac-depleted mice, related to **Figure 5.**

(A) Representative TEM images of mitochondria in the extracellular space, 21 days after cMac-depletion.

(B) Assessment of cardiac autophagy by measuring changes in LC3II/I ratios, Beclin1 and p62 proteins by western blot of heart extracts from wild-type controls (day 0) and cMac-depleted mice, for the indicated days. Bars show mean ± SEM from 3-7 mice per group, two independent experiments. *, $p<0.05$; **, $p<0.01$; ***, $p<0.001$ as determined by unpaired t-test.

(C) Autophagy flux in isolated cardiomyocytes from wild-type controls and cMac-depleted mice after two days of DT administration. Fluxes were measured by staining for LC3 (red) and nuclei (DAPI, blue) in basal and hydroxychloroquine (HCQ)-treated cells. Bars show mean ± SEM of LC3+ particles per cardiomyocyte; n = 3 mice per group. Scale bar, 20 µm. **, $p<0.01$; ***, $p<0.001$; n.s., not significant, as determined by Student t-test test.

(D) Left, experimental scheme to analyze autophagy and inflammasome markers in cMac-depleted mice (CD169^{DTR}+DT), treated or not with MCC950 for 21 days. Right, levels of the indicated proteins in heart (21 day depletion) extracts as measured by western blot analysis; n = 5 mice. *, $p>0.05$; **, $p<0.01$; ***, $p<0.001$, as determined by Student t-test test.

Controls for all cMac-depletion experiments were wild-type mice treated with DT.

Figure S6. Cardiac stress induces exopher production, related to **Figure 6.**

(A) Micrograph of infarcted areas in Card^RED mice after 7 days of permanent coronary artery ligation. Indicated are Infarct (inside dashed line) and Peri-infarct areas. Scale bar, 100 μm.

(B) Representative micrographs of exopher-like structures (arrowheads) and cMacs in remote and peri-infarct areas of infarcted hearts. Bar graph at right shows mean ± SEM number of exopher-like particles per mm^2 of cardiomyocyte-occupied area; data from 3 mice per group. ***, $p<0.01$, as determined by the Student's t-test. Scale bar, 20 μm.

(C) Micrographs of exopher-like particles (yellow arrowheads) in infarcted myocardia, showing positive staining for Ndufs2, and negative for F-actin. Scale bar, 10 μm.

(D-E) Effect of cMac depletion during isoproterenol-induced stress. **(D)** Top, experimental scheme to analyze cardiac function and markers associated with cardiac damage in Control and cMac-depleted mice, treated with ISO or vehicle once per day during 7 days. Bottom, selected cardiac parameters measured by echocardiography. Bar graphs show mean ± SEM values normalized to the control group (WT+DT without ISO); data from at least 7 mice per group. *, $p<0.05$; **, $p<0.01$; ***, $p<0.001$ as determined by ANOVA with Dunn's multiple comparisons test. LV, left ventricle; Vol, volume; EF, ejection fraction. **(E)** Levels of total creatine kinase (CK) and cardiac-specific isoform (CK-MB) in plasma of control and cMac depleted mice after 7 days of ISO administration. Values shown as box and whiskers, from 7 mice per group. *, $p<0.05$; ***, $p<0.001$ by ANOVA with Dunn's multiple comparisons test.

(F) Survival curves of control and cMac-depleted mice subjected to myocardial infarction with reperfusion 2 days after a single DT dose. P-value is calculated by Log-rank for Mantel-Cox survival curves; data from 10-15 mice per group and two independent experiments.

Controls for all cMac-depletion experiments were wild-type mice treated with DT.

Figure S7. Mertk is a phagocytic receptor for cardiac exophers, related to **Figure 7**.

(A) Expression of Mertk in cardiac cells. tSNE plots show expression of *Cx3cr1* (left) to identify cMacs, and Mertk, as defined from scRNAseq from the Tabula Muris Consortium. Note the predominant expression of Mertk in cMacs.

(B) Heatmaps showing differential expression of phagocytosis-related genes and Myh6 (negative control) in cMacs vs microglia and splenic macrophages. Analyses were performed from public databases (Pinto et al., 2012).

(C) Bar Graph shows cMacs numbers per g of cardiac tissue in Mertk$^{-/-}$ and WT mice. *, p<0.05; as determined by unpaired t-test.

(D) Representative Western Blot (Top) and levels of different NLRP3 inflammasome related-proteins in heart extracts of wild type and Mertk$^{-/-}$ mice, as measured by western blot. Bar graphs show mean ± SEM protein levels. Data from 6 mice per group. **, p<0.01; ***, p<0.001 as determined by unpaired t-test.

(E) Levels of different autophagy related-proteins in heart extracts of wild type and Mertk$^{-/-}$ mice, as measured by western blot. Bar graphs show mean ± SEM protein levels. Data from 6 mice per group. **, p<0.01; ***, p<0.001 as determined by unpaired t-test.

(F) Autophagy flux in isolated cardiomyocytes from wild type and Mertk$^{-/-}$ mice. Fluxes were measured by staining for LC3 (red) and nuclei (DAPI, blue) in basal and Hydroxychloroquine (HCQ)-treated cells. Bars show mean ± SEM of LC3+ particles per cardiomyocyte. n = 3 mice per group. Scale bar, 20 μm. *, p<0.05; ***, p<0.001; n.s., not significant, as determined by ANOVA.

(G) Mitochondrial content as determined by Tom20 immunofluorescence analysis. Bars show mean ± SEM from n= 5 mice per group; **, p<0.01; as determined by unpaired t-test.

(H) Ex vivo ATP production rates in isolated mitochondria in wild-type or Mertk$^{-/-}$ mice at different ages in the presence of the indicated substrates (glutamate + malate, or succinate). ATP values are corrected to CS activity and presented as Box and Whiskers; data from 10-12 mice per group. *, p<0.05; n.s, not significant, as determined by unpaired t-test.

(I) Diastolic Function, as measured by the ratio between the E and A mitral valve waves in 8-10 weeks old animals. Bars show mean ± SEM from n= 20-24 mice per group; **, p<0.01; as determined by unpaired t-test

Supplemental videos legends

Video S1: Optical sectioning and distribution of cMacs in a CX3CR1^{GFP} heart, Related to **Figure 1**.

First part: Optical sections generated by light sheet microscopy of the heart of a heterozygous CX3CR1^{GFP} mouse after clarification; note that many cMacs (green dots) populate the myocardial sections. Second part: 3D view of the heart of a heterozygous CX3CR1^{GFP} mouse after clarification; note the dense network of cMacs (green) within the myocardial mass. Vessels are shown in white (CD31 staining) to better appreciate the anatomy of the heart.

Video S2: Distribution of cMacs around individual cardiomyocytes, Related to **Figure 1**.

3D imaging of hearts from inducible αMHC^{CRE-ERT}; Rosa26^{TdTom} reporter mice after low-dose tamoxifen, which allows generation of mosaic mice containing only a small fraction of cardiomyocytes expressing tdTomato (red). cMac staining with anti-CD68 (green) in these mice allows visualizing the number and distribution of cMacs around isolated cardiomyocytes in naive hearts. Autofluorescence (purple) shows the actual structure of non-labelled cardiomyocytes.

Video S3. cMacs engulf cardiomyocyte-derived exophers containing mitochondria, Related to **Figure 2**.

Reconstruction and 3D view of heart slices from αMHC^{CRE}; Rosa26^{TdTom} (Card^{RED}) mice were exophers (red), derived from cardiomyocytes (large cells; red), have been captured by surrounding cMacs (green). In the second part of the video we introduce Tom20 staining (white) to show the presence of mitochondria inside the captured exophers. Nuclei are labelled with DAPI (blue).

Video S4. Uptake of cardiomyocyte-derived mitochondria into LAMP1+ phagolysosomes in cMacs, Related to **Figure 3**.

Reconstruction and 3D view of the myocardium of a mouse infected with AAV9-mtKeima vector. The reconstruction shows mt-Keima-tagged mitochondria derived from a cardiomyocyte (red) that have been phagocytosed by a cMac (green). Note that the mitochondria is contained inside a Lamp1+ lysosomal compartment (white). Nuclei are labelled with DAPI (blue), and autofluorescence is used to visualize cardiomyocytes (cyan).

Videos S5. Cardiomyocyte and cMac coculture, Related to **Figure 3**.

Time-lapse video of cardiomyocytes (HI1^{GFP} cell line, in green) and cMacs (sorted from DsRed mice, in red) co-cultured for two hours. Yellow arrows indicate cardiomyocyte-derived exophers. Scale bar is 20 μm.

Supplemental tables and legends

Supplemental Table 1. Serum biochemical parameters and Leukocyte counts in the blood and hearts of Control and cMac depleted mice. Related to Figure 1. Control (Wild Type + DT) and cMac depleted (CD169[DTR] +DT) mice were treated with DT (see Methods section) and analysed at day 21 after treatment. Values are mean ± SEM from 6-11 mice per group.

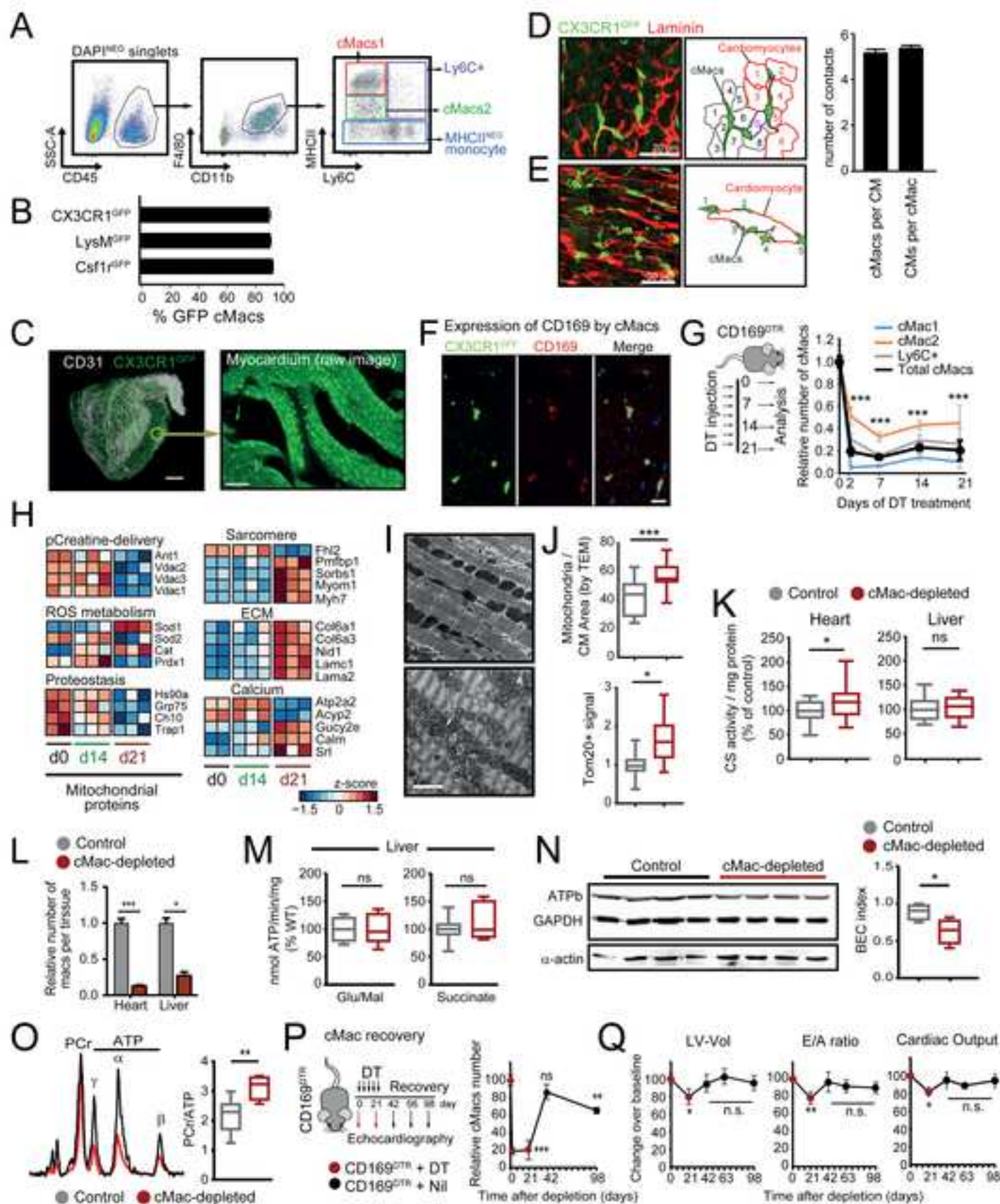| Parameter	Units	Control	cMac Depleted (day 21)	P value
Total serum proteins	mg/dL	6.04 ± 0.11	6.43 ± 0.27	0.243
C-reactive protein	mg/dL	0.15 ± 0.04	0.16 ± 0.06	0.849
LDH	U/L	402.71 ± 197.96	4391.86 ± 924.86	**
AST/GOT	U/L	108.71 ± 19.80	422.86 ± 156.92	**0.091**
Creatine Kinase MB	U/L	142.57 ± 18.83	781.14 ± 242.89	*
Creatine kinase	U/L	295.00 ± 81.49	1566.57 ± 538.81	**0.052**
Creatinine	mg/dL	0.34 ± 0.03	0.10 ± 0.04	**
Alkaline phosphatase	U/L	21.57 ± 5.00	79.43 ± 14.75	**
Potassium	mmol/L	33.37 ± 1.40	35.70 ± 1.99	0.393
Chlorine	mmol/L	108.57 ± 2.35	104.71 ± 2.50	0.319
Sodium	mmol/L	144.29 ± 1.21	146.57 ± 2.51	0.463
Iron	μg/dL	23.00 ± 2.51	36.43 ± 7.24	0.130
Lymphocytes (Blood)	cells/mL	7457 ± 798	7656 ± 751	0.875
Neutrophils (Blood)	cells/mL	2347 ± 630	3653 ± 545	0.180
Monocytes (Blood)	cells/mL	338 ± 57	417 ± 102	0.615
Neutrophils (Heart)	cells/0.1 mg	16418 ± 3967	27610 ± 3951	0.086
Ly6C[HI] Monocytes (Heart)	cells/0.1 mg	2734 ± 779	3895 ± 519	0.273
Ly6C[LO] Monocytes (Heart)	cells/0.1 mg	5669 ± 1405	7413 ± 1621	0.466
cMacs (Heart)	cells/0.1 mg	37746 ± 1808	8329 ± 1754	<0.001***

AST/GOT: Aspartate aminotransferase; LDH: Lactate Dehydrogenase; Creatine Kinase MB: ("myocardial band").

Supplemental Table 2. Description of patient used for cardiac tissue analysis.
Related to STAR Methods.

Patient no.	1	2	3	4	5
Age (years)	55	72	74	75	62
Sex	Female	Female	Male	Female	Female
LVEF	Normal	Normal	Normal	Normal	Normal
Indication for surgery	Mitral regurgitation	Mitral regurgitation	Mitral regurgitation	Mitral stenosis	Mitral regurgitation
Bypass time (min)	96	102	80	66	85
Crossclamp time (min)	75	81	60	55	74

LVEF: left ventricle ejection fraction.
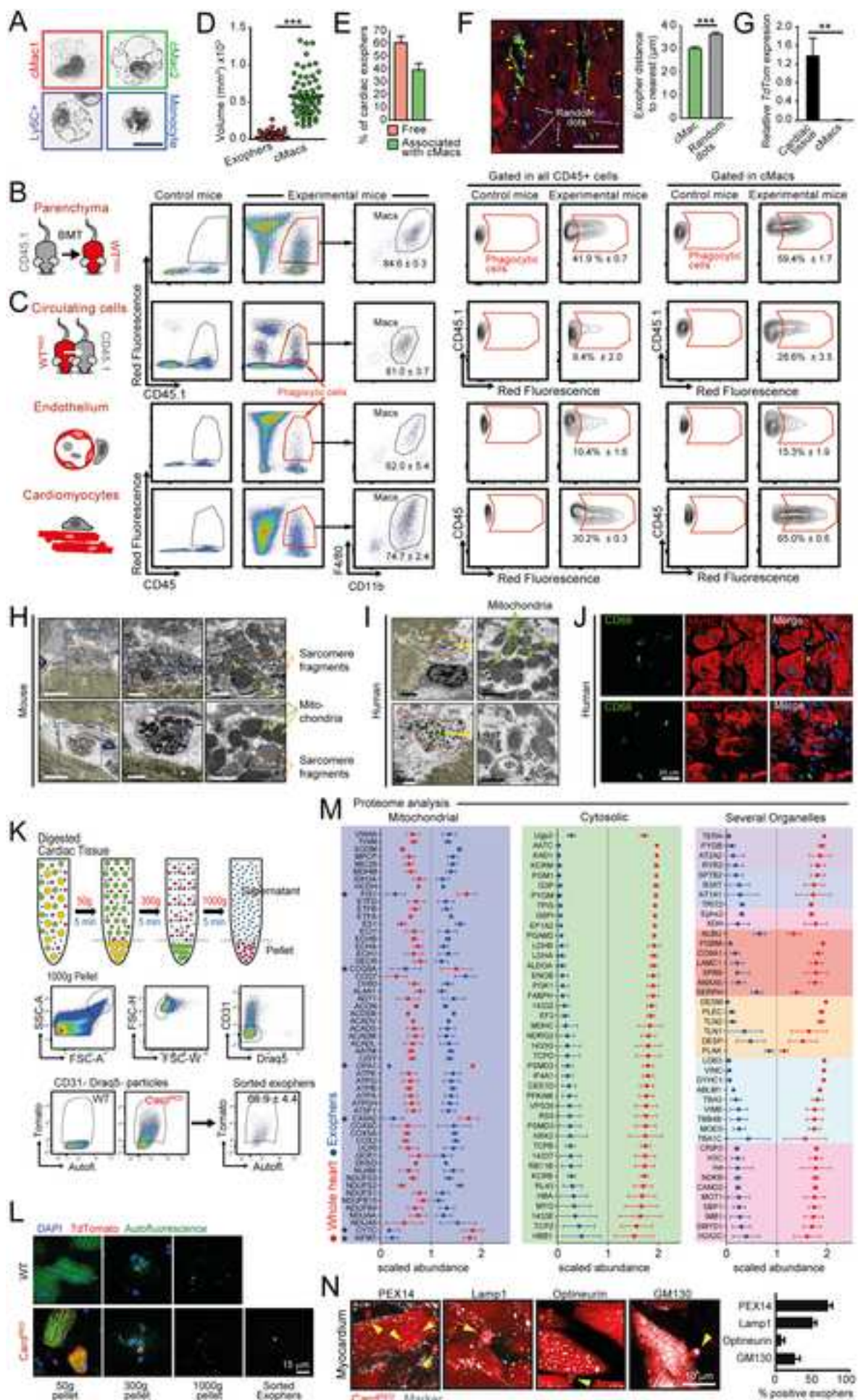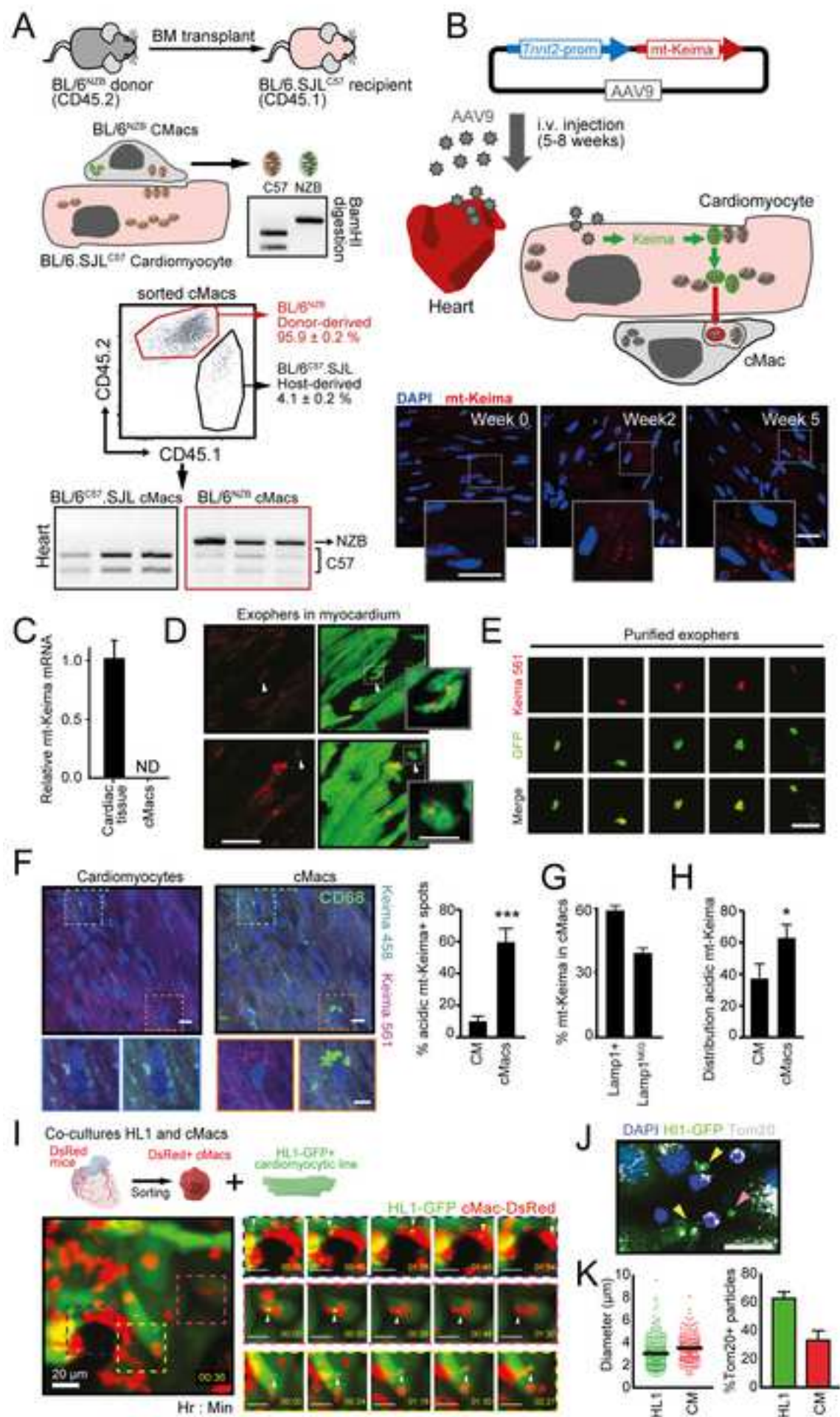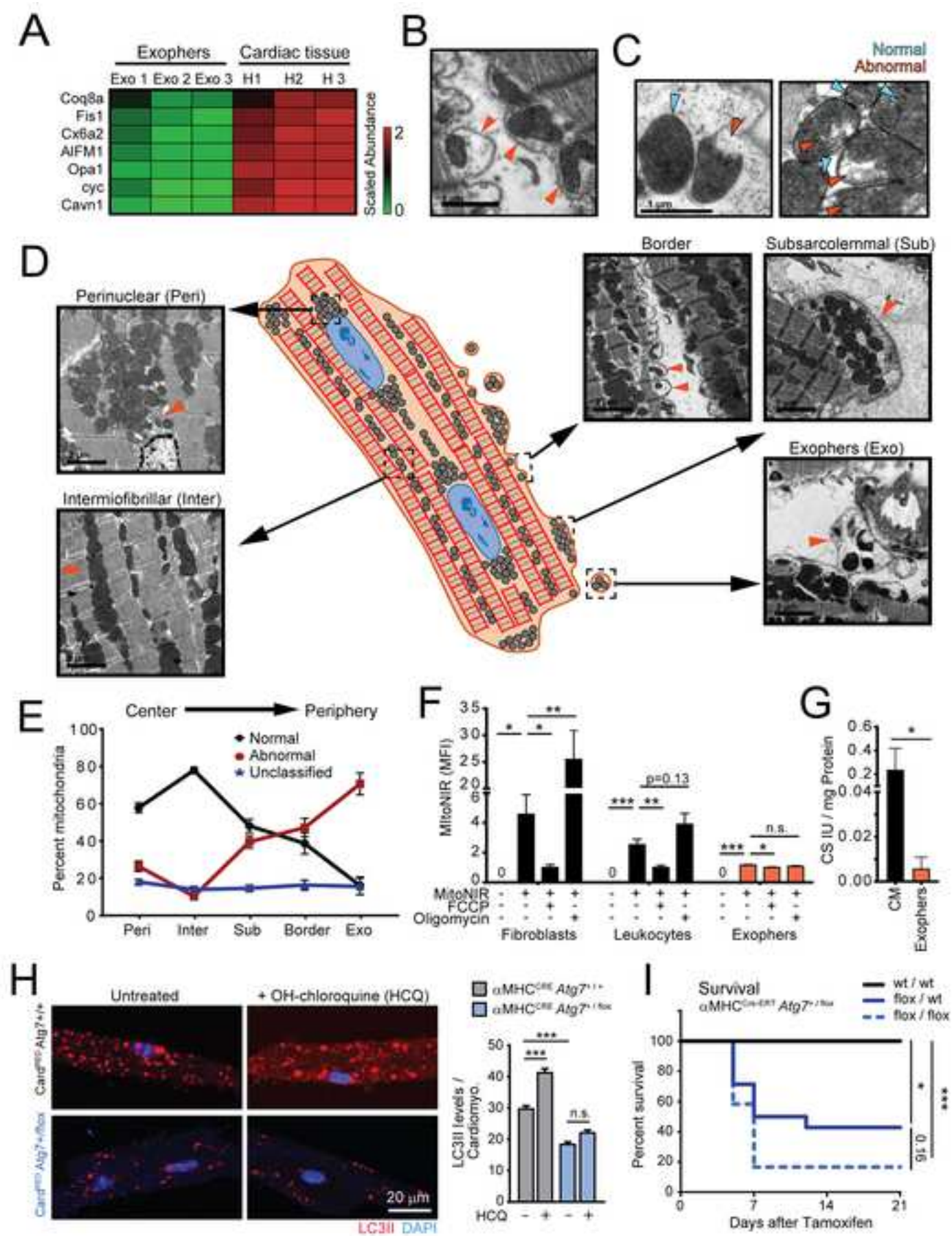
A cMac-depleted hearts (day 21)

B LC3II/I Ratio   Beclin1   p62

Arbitrary Units normalized to day 0

☐ day 0 ☐ day 7 ☐ day 14 ☐ day 21

C Autophagy flux

Untreated   OH-chloroquine (HCQ)   day 2

control

cMac-depl.

LC3II DAPI   20 µm

☐ No depleted ☐ cMac-depleted (day 2)

LC3 II levels / Cardiomyo.

HCQ − + − +

D

CD169^DTR

DT and PBS/MCC950

0 7 14 21 day

Analysis

● cMac-depleted + PBS
● cMac-depleted + MCC950

Arbitrary Units

NLRP3 Caspase-1 p62

A Miocardial Infarction (Card^RED mice) — tdTomato CD68 — Peri-infarct — Infarcted — 100 μm

B Peri-Infarct — Remote — tdTomato CD68 — 20 μm — Exopher-like structures / mm² of tdTomato+ area (x10²) — Remote — Peri-infarct — ***

C Exophers in myocardial Infarction — Exophers — Ndufs2 — F-Actin — 10 μm

D WT and CD169^DTR — DT ± ISO — 0 — 7 day — Echocardiography 18h after last ISO — LV-Vol (μl) — E/A ratio — Ejection Fraction — Cardiac Output (ml/min) — Data normalized to Untreated Control group — cMac depl. — ISO

E Isoproterenol-treatment — U/L plasma — CK — CK-MB — ISO control — ISO + cMac-depleted — *** *

F Myocardial infarction — % Survival — Days after infarction — Control — cMac-depleted — p<0.001